

1 **Interannual snow accumulation variability on glaciers derived from repeat, spatially**  
2 **extensive ground-penetrating radar surveys**

3

4 Daniel McGrath<sup>1</sup>, Louis Sass<sup>2</sup>, Shad O’Neel<sup>2</sup> Chris McNeil<sup>2</sup>, Salvatore G. Candela<sup>3</sup>,  
5 Emily H. Baker<sup>2</sup>, and Hans-Peter Marshall<sup>4</sup>

6 <sup>1</sup>*Department of Geosciences, Colorado State University, Fort Collins, CO*

7 <sup>2</sup>*U.S. Geological Survey Alaska Science Center, Anchorage, AK*

8 <sup>3</sup>*School of Earth Sciences and Byrd Polar Research Center, Ohio State University,*  
9 *Columbus, OH*

10 <sup>4</sup>*Department of Geosciences, Boise State University, Boise, ID*

11 **Abstract**

12 There is significant uncertainty regarding the spatiotemporal distribution of seasonal  
13 snow on glaciers, despite being a fundamental component of glacier mass balance. To  
14 address this knowledge gap, we collected repeat, spatially extensive high-frequency  
15 ground-penetrating radar (GPR) observations on two glaciers in Alaska during the spring  
16 of five consecutive years. GPR measurements showed steep snow water equivalent  
17 (SWE) elevation gradients at both sites; continental Gulkana Glacier’s SWE gradient  
18 averaged 115 mm 100 m<sup>-1</sup> and maritime Wolverine Glacier’s gradient averaged 440 mm  
19 100 m<sup>-1</sup> (over >1000 m). We extrapolated GPR point observations across the glacier  
20 surface using terrain parameters derived from digital elevation models as predictor  
21 variables in two statistical models (stepwise multivariable linear regression and  
22 regression trees). Elevation and proxies for wind redistribution had the greatest  
23 explanatory power, and exhibited relatively time-constant coefficients over the study  
24 period. Both statistical models yielded comparable estimates of glacier-wide average  
25 SWE (1 % average difference at Gulkana, 4 % average difference at Wolverine),  
26 although the spatial distributions produced by the models diverged in unsampled regions  
27 of the glacier, particularly at Wolverine. In total, six different methods for estimating the  
28 glacier-wide winter balance average agreed within ± 11 %. We assessed interannual  
29 variability in the spatial pattern of snow accumulation predicted by the statistical models  
30 using two quantitative metrics. Both glaciers exhibited a high degree of temporal  
31 stability, with ~85 % of the glacier area experiencing less than 25 % normalized absolute  
32 variability over this five-year interval. We found SWE at a sparse network (3 stakes per  
33 glacier) of long-term glaciological stake sites to be highly correlated with the GPR-  
34 derived glacier-wide average. We estimate that interannual variability in the spatial  
35 pattern of winter SWE accumulation is only a small component (4–10 % of glacier-wide  
36 average) of the total mass balance uncertainty and thus, our findings support the concept

37 that sparse stake networks effectively measure interannual variability in winter balance  
38 on glaciers, rather than some temporally varying spatial pattern of snow accumulation.

39

## 40 **1. Introduction**

41 Our ability to quantify glacier mass balance is dependent on accurately resolving the  
42 spatial and temporal distributions of snow accumulation and snow/ice ablation.

43 Significant advances in our knowledge of ablation processes have improved  
44 observational and modelling capacities (Hock, 2005; Huss and Hock, 2015; Fitzpatrick et  
45 al., 2017), yet comparable advances in our understanding of the distribution of snow  
46 accumulation have not kept pace (Hock et al., 2017). Reasons for this discrepancy are  
47 two-fold: (i) snow accumulation exhibits higher variability than ablation, both in  
48 magnitude and length scale, largely due to wind redistribution in the complex high-relief  
49 terrain where mountain glaciers are typically found (Kuhn et al., 1995) and (ii)  
50 accumulation observations are typically less representative (i.e., one stake in a few  
51 hundred meter elevation band) or less effective than comparable ablation observations  
52 (i.e., precipitation gage measuring snowfall vs. radiometer measuring short-wave  
53 radiation). This discrepancy presents a significant limitation to process-based  
54 understanding of mass balance drivers. Furthermore, a warming climate has already  
55 modified – and will continue to modify – the magnitude and spatial distribution of snow  
56 on glaciers through a reduction in the fraction of precipitation falling as snow and an  
57 increase in rain-on-snow events (Knowles et al., 2006; McAfee et al., 2013; Klos et al.,  
58 2014; McGrath et al., 2017; Littell et al., 2018).

59

60 Significant research has been conducted on the spatial and, to a lesser degree, the  
61 temporal variability of seasonal snow in mountainous and high-latitude landscapes (e.g.,  
62 Balk and Elder, 2000; Molotch et al., 2005; Erickson et al., 2005; Deems et al., 2008;  
63 Sturm and Wagner, 2010; Schirmer et al., 2011; Winstral and Marks, 2014; Anderson et  
64 al., 2014; Painter et al., 2016). Although major advances have occurred in applying  
65 physically-based snow distribution models (i.e., iSnobal (Marks et al., 1999), SnowModel  
66 (Liston and Elder, 2006), Alpine 3D (Lehning et al., 2006)), the paucity of required  
67 meteorological forcing data proximal to glaciers limits widespread application. Many  
68 other studies have successfully developed statistical approaches that rely on the

69 relationship between the distribution of snow water equivalent (SWE) and physically-  
70 based terrain parameters (also referred to as physiographic or topographic properties or  
71 variables) to model the distribution of SWE across entire basins (e.g., Molotch et al.,  
72 2005; Anderson et al., 2014; Sold et al., 2013; McGrath et al., 2015).

73

74 A major uncertainty identified by these studies is the degree to which these statistically  
75 derived relationships remain stationary in time. Many studies (Erickson et al., 2005;  
76 Deems et al., 2008; Sturm and Wagner, 2010; Schirmer et al., 2011; Winstral and Marks,  
77 2014; Helfricht et al., 2014) have found ‘time-stability’ in the distribution of SWE,  
78 including locations where wind redistribution is a major control on this distribution. For  
79 instance, a climatological snow distribution pattern, produced from the mean of nine  
80 standardized surveys, accurately predicted the observed snow depth in a subsequent  
81 survey in a tundra basin in Alaska (~4–10 cm root mean square error; Sturm and Wagner,  
82 2010). Repeat LiDAR surveys over two years at three hillslope-scale study plots in the  
83 Swiss Alps found a high degree of correlation ( $r=0.97$ ) in snow depth spatial patterns  
84 (Schirmer et al., 2011). They found that the final snow depth distributions at the end of  
85 the two winter seasons were more similar than the distributions of any two individual  
86 storms during that two-year period (Schirmer et al., 2011). Lastly, an 11-year study of  
87 extensive snow probing (~1200 point observations) at a 0.36 km<sup>2</sup> field site in  
88 southwestern Idaho found consistent spatial patterns ( $r=0.84$ ; Winstral and Marks, 2014).  
89 Collectively, these studies suggest that in landscapes characterized by complex  
90 topography and extensive wind redistribution of snow, spatial patterns are largely time-  
91 stable or stationary, as long as the primary drivers are stationary.

92

93 Even fewer studies have explicitly examined the question of interannual variability in the  
94 context of snow distribution on glaciers. Spatially-extensive snow probe datasets are  
95 collected by numerous glacier monitoring programs (e.g., Bauder et al., 2017; Kjølmoen  
96 et al., 2017; Escher-Vetter et al., 2009) in order to calculate a winter mass balance  
97 estimate. Although extensive, such manual approaches are still limited by the number of  
98 points that can be collected and uncertainties in correctly identifying the summer surface  
99 in the accumulation zone, where seasonal snow is underlain by firn. One study of two

100 successive end-of-winter surveys of snow depth using probes on a glacier in Svalbard  
101 found strong interannual variability in the spatial distribution of snow, and the  
102 relationship between snow distribution and topographic features (Hodgkins et al., 2006).  
103 Elevation was found to only explain 38–60 % of the variability in snow depth, and in one  
104 year, snow depth was not dependent on elevation in the accumulation zone (Hodgkins et  
105 al., 2006). Instead, aspect, reflecting relative exposure or shelter from prevailing winds,  
106 was found to be a significant predictor of accumulation patterns. In contrast, repeat  
107 airborne LiDAR surveys of a ~36 km<sup>2</sup> basin (~50% glacier cover) in Austria over five  
108 winters found that the glacierized area exhibited less interannual variability (as measured  
109 by the interannual standard deviation) than the non-glacierized sectors of the basin  
110 (Helfricht et al., 2014). Similarly, a three-year study of snow distribution on  
111 Findelgletscher in the Swiss Alps using ground-penetrating radar (GPR) found low  
112 interannual variability, as 86 % of the glacier area experienced less than 25 % normalized  
113 relative variability (Sold et al., 2016). These latter studies suggest that seasonal snow  
114 distribution on glaciers likely exhibits ‘time-stability’ in its distribution, but few datasets  
115 exist to robustly test this hypothesis.

116

117 The ‘time-stability’ of snow distribution on glaciers has particularly important  
118 implications for long-term glacier mass balance programs, as seasonal and annual mass  
119 balance solutions are derived from the integration of a limited number of point  
120 observations (e.g., 3 to 50 stakes), and the assumption that stake and snow pit  
121 observations accurately represent interannual variability in mass balance rather than  
122 interannual variability in the spatial patterns of mass balance. Previous work has shown  
123 ‘time-stability’ in the spatial pattern of annual mass balance (e.g., Vincent et al., 2017)  
124 and while this is important for understanding the uncertainties in glacier-wide mass  
125 balance estimates, the relative contributions of accumulation and ablation to this stability  
126 are poorly constrained, thereby hindering a process-based understanding of these spatial  
127 patterns. Furthermore, accurately quantifying the magnitude and spatial distribution of  
128 winter snow accumulation on glaciers is a prerequisite for understanding the water budget  
129 of glacierized basins, with direct implications for any potential use of this water, whether  
130 that be ecological, agricultural, or human consumption (Kaser et al., 2010).

131

132 To better understand the ‘time-stability’ of the spatial pattern of snow accumulation on  
133 glaciers, we present five consecutive years of extensive GPR observations for two  
134 glaciers in Alaska. First, we use these GPR-derived SWE measurements to train two  
135 different types of statistical models, which were subsequently used to spatially  
136 extrapolate SWE across each glacier’s area. Second, we assess the temporal stability in  
137 the resulting spatial distribution in SWE. Finally, we compare GPR-derived winter mass  
138 balance estimates to traditional glaciological derived mass balance estimates and quantify  
139 the uncertainty that interannual variability in spatial patterns in snow accumulation  
140 introduces to these estimates.

141

## 142 **2. Study Area**

143 During the spring seasons of 2013–2017, we conducted GPR surveys on Wolverine and  
144 Gulkana glaciers, located on the Kenai Peninsula and eastern Alaskan Range in Alaska  
145 (Fig. 1). These glaciers have been studied as part of the U.S. Geological Survey’s  
146 Benchmark Glacier project since 1966 (O’Neel et al., 2014). Both glaciers are ~16 km<sup>2</sup> in  
147 area and span ~1200 m in elevation (426 – 1635 m asl for Wolverine, 1163 – 2430 m asl  
148 for Gulkana). Wolverine Glacier exists in a maritime climate, characterized by warm air  
149 temperatures (mean annual temperature = –0.2 °C at 990 meters; median equilibrium line  
150 altitude for 2008 – 2017 is 1235 m asl) and high precipitation (median glacier-wide  
151 winter balance = 2.0 m water equivalent (m w.e.)), while Gulkana is located in a  
152 continental climate, characterized by colder air temperatures (mean annual temperature =  
153 –2.8 °C at 1480 meters; median equilibrium line altitude for 2008 – 2017 is 1870 m asl)  
154 and less precipitation (median glacier-wide winter balance = 1.2 m w.e.) (Fig. 2). The  
155 cumulative mass balance time series for both glaciers is negative (~ –24 m w.e. between  
156 1966–2016), with Gulkana showing a more monotonic decrease over the entire study  
157 interval, while Wolverine exhibited near equilibrium balance between 1966 and 1987,  
158 and sharply negative to present (O’Neel et al., 2014; O’Neel et al., 2018).

159

## 160 **3. Methods**

161 The primary SWE observations are derived from a GPR measurement of two-way travel  
162 time (*twt*) through the annual snow accumulation layer. We describe five main steps to  
163 convert *twt* along the survey profiles to annual distributed SWE products for each glacier.  
164 These include (i) acquisition of GPR and ground-truth data, (ii) calculation of snow  
165 density and associated radar velocity, which are used to convert measured *twt* to annual  
166 layer depth and subsequently SWE, and (iii) application of terrain parameter statistical  
167 models to extrapolate SWE across the glacier area. We then describe approaches to (iv)  
168 evaluate the temporal consistency in spatial SWE patterns and (v) compare GPR-derived  
169 SWE and direct (glaciological) winter mass balances.

170

### 171 **3.1. Radar data collection and processing**

172 Common-offset GPR surveys were conducted with a 500 MHz Sensors and Software  
173 Pulse Ekko Pro system in late spring close to maximum end-of-winter SWE and prior to  
174 the onset of extensive surface melt. GPR parameters were set to a waveform-sampling  
175 rate of 0.1 ns, a 200-ns time window, and “Free Run” trace increments, where samples  
176 are collected as fast as the processor allows, instead of at uniform temporal or spatial  
177 increments.

178

179 In general, GPR surveys were conducted by mounting a plastic sled behind a snowmobile  
180 and driving at a near-constant velocity of 15 km h<sup>-1</sup> (Fig. 3, S1, S2), resulting in a trace  
181 spacing of ~20 cm. Coincident GPS data were collected using a Novatel Smart-V1 GPS  
182 receiver (Omnistar corrected, L1 receiver with root-mean-square accuracy of 0.9 m  
183 (Perez-Ruiz et al., 2011)). We collected a consistent survey track from year-to-year that  
184 minimized safety hazards (crevasses, avalanche runouts) but optimized the sampling of  
185 terrain parameter space on the glacier (e.g., range and distribution of elevation, slope,  
186 aspect, curvature, etc.). However, in 2016 at Wolverine Glacier, weather conditions and  
187 logistics did not allow for ground surveys to be completed. Instead, a number of radar  
188 lines were collected via a helicopter survey. To best approximate the ground surveys  
189 completed in other years, we selected a subset of helicopter GPR observations within 150  
190 m of the ground-based surveys. Previous comparisons between ground and helicopter

191 platforms found excellent agreement in SWE point observations (coefficient of  
192 determination ( $R^2$ )=0.96, root mean square error=0.14 m; McGrath et al., 2015).

193

194 Radargrams were processed using the ReflexW-2D software package (Sandmeier  
195 Scientific Software). All radargrams were corrected to time zero, taken as the first  
196 negative peak in the direct wave (Yelf and Yelf, 2006), and a dewow filter (mean  
197 subtraction) was applied over 2 ns. When reflectors from the base of the seasonal snow  
198 cover were insufficiently resolved, gain and band-pass filters were subsequently applied.  
199 Layer picking was guided by ground-truth efforts and done semi-automatically using a  
200 phase-following layer picker. For further details, please see McGrath et al. (2015).

201

### 202 **3.2. Ground truth observations**

203 We collected extensive ground-truth data to validate GPR surveys, including probing and  
204 snowpit/cores. In the ablation zone of each glacier, we probed the snowpack thickness  
205 every ~500 m along-track. In addition, we measured seasonal snow depth and density at  
206 an average of five locations (corresponding to the glaciological observations; see Section  
207 3.5) on each glacier in each year. Typically these locations include one or two in the  
208 ablation zone, one near the long-term ELA, and two or more in the accumulation zone.  
209 We measured snow density using a gravimetric approach in snowpits (at 10 cm intervals)  
210 and with 7.25 cm diameter cores (if total depth >2 m; at 10–40 cm intervals depending on  
211 natural breaks) to the previous summer surface. We calculated a density profile and  
212 column-average density,  $\rho_{site}$ , at each site.

213

214 As snow densities did not exhibit a consistent spatial nor elevation dependency on the  
215 glaciers (e.g., Fausto et al., 2018), we calculated a single average density,  $\rho$ , of all  $\rho_{site}$   
216 on each glacier and each year, which was subsequently used to calculate SWE:

217

$$218 \quad SWE = \left(\frac{twt}{2}\right) \cdot v_s \cdot \rho. \quad (1)$$

219

220 where  $twt$  is the two-way travel time as measured by the GPR and  $v_s$  is the radar  
221 velocity.  $v_s$  was calculated for each glacier in each year as the average of two

222 independent approaches: (i) an empirical relationship based on the glacier-wide average  $\rho$   
223 (Kovacs et al., 1995) and (ii) a least-squares regression between snow depth derived by  
224 probing and all radar *twt* observations within a 3-m radius of the probe site. An  
225 exception was made at Wolverine in 2016 as no coincident probe depth observations  
226 were made during the helicopter-based surveys. Instead, we estimated the second radar  
227 velocity by averaging radar velocities calculated from observed *twt* and snow depths at  
228 three snowpit/core locations.

229

### 230 **3.3. Spatial Extrapolation**

231 Extrapolating SWE from point measurements to the basin scale has been a topic of  
232 focused research for decades (e.g., Woo and Marsh, 1978; Elder et al., 1995; Molotch et  
233 al., 2005). Most commonly, the dependent variable SWE is related to a series of  
234 explanatory terrain parameters, which are proxies for the physical processes that actually  
235 control SWE distribution across the landscape. These include orographic gradient in  
236 precipitation (elevation), wind redistribution of existing snow (slope, curvature, drift  
237 potential), and aspect with respect to solar radiation and prevailing winds (eastness,  
238 northness). We derived terrain parameters from 10-m resolution digital elevation models  
239 (DEMs) sourced from the ArcticDEM project (Noh and Howat, 2015) for Gulkana and  
240 produced from airborne Structure from Motion photogrammetry at Wolverine (Nolan et  
241 al., 2015). Both DEMs were based on imagery from August 2015. Specifically, these  
242 parameters include elevation, surface slope, surface curvature, northness (Molotch et al.,  
243 2005), eastness, and snow drift potential (*Sb*) (Winstral et al., 2002; Winstral et al., 2013;  
244 Fig. S3, S4). The *Sb* parameter is commonly used to identify locations where airflow  
245 separation occurs based on both near and far-field topography and are thus likely  
246 locations to accumulate snow drifts (Winstral et al., 2002). For specific details on this  
247 calculation, please refer to Winstral et al. (2002). In the application of *Sb* here, we  
248 determined the principle direction by calculating the modal daily wind direction during  
249 the winter (October – May) when wind speeds exceeded  $5 \text{ m s}^{-1}$  (~minimum wind  
250 velocity for snow transport; Li and Pomeroy, 1997). The length scales for curvature were  
251 found using an optimization scheme that identified the highest model  $R^2$ .

252



253 Prior to spatial extrapolation, we aggregated GPR observations to the resolution of the  
254 DEM by calculating the median value of all observations within each 10 m pixel of the  
255 DEM. We then utilized two approaches to extrapolate GPR point observations across the  
256 glacier surface: (i) least-squares elevation gradient applied to glacier hypsometry and (ii)  
257 statistical models. For (i), we derived SWE elevation gradients in two ways; first, solely  
258 on observations that followed the glacier centerline and second, from the entire spatially-  
259 extensive dataset. For (ii), we utilized both stepwise multivariable linear regressions and  
260 regression trees (Breiman et al., 1984). All of these approaches produced a spatially-  
261 distributed SWE field over the entire glacier area. Individual points in this field are  
262 equivalent to point winter balances ( $b_w$ ; m w.e.). From the distributed  $b_w$  field, we  
263 calculated a mean area-averaged winter balance ( $B_w$ ; m w.e.).

264

265 Additionally, we implemented a cross-validation approach to the statistical extrapolations  
266 (multivariable regression and regression tree), whereby 75 % of the aggregated  
267 observations were used for training and 25 % were used for testing. However, rather than  
268 randomly selecting pixels from across the entire dataset, we randomly selected a single  
269 pixel containing aggregated GPR observations and then extended this selection out along  
270 continuous survey lines until we reached 25 % of the total observational dataset, thus  
271 removing entire sections (and respective terrain parameters) from the analysis (Fig. S5).  
272 This approach provided a more realistic test for the statistical models, as the random  
273 selection of individual cells did not significantly alter terrain-parameter distributions. For  
274 each glacier and each year, we produced 100 training/test dataset combinations, but rather  
275 than take the single model with the highest  $R^2$  or lowest RMSE from the resulting test  
276 dataset, we produced a distributed SWE product by taking the median value for each  
277 pixel from all 100 model runs and a glacier-wide median value that is the median of all  
278 100 individual  $B_w$  estimates. We chose the median-value approach over a highest  
279  $R^2$ /lowest RMSE approach that is often utilized because, despite being randomly  
280 selected, some training datasets were inherently advantaged by a more complete  
281 distribution of terrain parameters. These iterations resulted in the highest  $R^2$ /lowest  
282 RMSE when applied to the training dataset, but weren't necessarily indicative of a better  
283 model.

284

### 285 **3.3.2. Stepwise Multivariable Linear Regression**

286 We used a stepwise multivariable linear regression model of the form,

$$287 \text{SWE}_{(i,j)} = c_1x_{1(i,j)} + c_2x_{2(i,j)} + \dots + c_nx_{n(i,j)} + \varepsilon_{(i,j)}, \quad (2)$$

288 where  $\text{SWE}_{(i,j)}$  is the predicted (standardized) value at location  $i,j$  and  $c_1, c_2, c_n$  are the beta  
289 coefficients of the model,  $x_1, x_2, x_n$  are terrain parameters which are independent variables  
290 that have been standardized and  $\varepsilon$  is the residual. We applied the regression model  
291 stepwise and included an independent variable if it minimized the Akaike information  
292 criterion (AIC; Akaike, 1974). We present the beta coefficients from each regression  
293 (each year, each glacier) to explore the temporal stability of these terms.

294

### 295 **3.3.3. Regression Trees**

296 Regression trees (Breiman et al., 1984) provide an alternative statistical approach for  
297 extrapolating point observations by recursively partitioning SWE into progressively more  
298 homogenous subsets based on independent terrain parameter predictors (Molotch et al.,  
299 2005; Meromy et al., 2013; Bair et al., 2018). The primary advantage of the regression  
300 tree approach is that each terrain parameter is used multiple times to partition the  
301 observations, thereby allowing for non-linear interactions between these terms. In  
302 contrast, the MVR only allows for a single “global” linear relationship for each parameter  
303 across the entire parameter-space. We implemented a random forest approach (Breiman,  
304 2001) of repeated regression trees (100 learning cycles) in Matlab, using weak learners  
305 and bootstrap aggregating (bagging; Breiman, 1996). Each weak learner omits 37% of  
306 observations, such that these “out-of-bag” observations are used to calculate predictor  
307 importance. The use of this ensemble/bagging approach reduces overfitting and thus  
308 precludes having to subjectively prune the tree and provides more accurate and unbiased  
309 error estimates (Breiman, 2001). Prior to implementing the regression tree, we removed  
310 the SWE elevation gradient from the observations using a least-squares regression. As  
311 described in the results, elevation is the dominant independent variable and as our  
312 observations (particularly at Wolverine) did not cover the entire elevation range, the  
313 regression tree approach was not well suited to predicting SWE at elevations outside of  
314 the observational range.

315

### 316 **3.4. Interannual variability in spatial patterns**

317 We quantified the stability of spatial patterns in SWE across the five-year interval using  
318 two approaches: (i) normalized range and (ii) the coefficient of determination. In the first  
319 approach, we first divided each pixel in the distributed SWE fields by the glacier-wide  
320 average,  $B_w$ , for each year and each glacier, and then calculated the range in these  
321 normalized values over the entire five-year interval. For example, if a cell has normalized  
322 values of 84 %, 92 %, 106 %, 112 % and 120 %, the normalized range would be 36 %. A  
323 limitation of this approach is that it is highly sensitive to outliers, such that a single year  
324 can substantially increase this range. This is similar to an approach presented by Sold et  
325 al. (2016), but unlike their calculation (their Fig. 9), the normalized values reported here  
326 have not been further normalized by the normalized mean of that pixel over the study  
327 interval. Thus, the values reported here are an absolute normalized range, whereas Sold et  
328 al. (2016) report a relative normalized range. In the coefficient of determination ( $R^2$ )  
329 approach, we computed the least-squares regression correlation between the SWE in each  
330 pixel and the glacier-wide average,  $B_w$ , derived from the MVR model over the five-year  
331 period. For this approach, cells with a higher  $R^2$  scale linearly with the glacier-wide  
332 average, while those with low  $R^2$  do not.

333

### 334 **3.5. Glaciological mass balance**

335 Beginning in 1966, glacier-wide seasonal (winter,  $B_w$ ; summer,  $B_s$ ) and annual balances ( $B_a$ )  
336 were derived from glaciological measurements made at three fixed locations on each glacier.  
337 The integration of these point measurements was accomplished using a site-index method –  
338 equivalent to an area-weighted average (March and Trabant, 1996; van Beusekom et al., 2010).  
339 Beginning in 2009, a more extensive stake network of seven to nine stakes was established on  
340 each glacier, thereby facilitating the use of a balance profile method for spatial extrapolation  
341 (Cogley et al., 2011). Systematic bias in the glaciological mass balance time-series is removed  
342 via a geodetic adjustment derived from DEM differencing over decadal timescales (e.g.,  
343 O’Neel et al., 2014). For this study, glaciological measurements were made within a day of the  
344 GPR surveys, and integrated over the glacier hypsometry using both the historically applied  
345 site-index method (based on the long-term three stake network) and the more commonly

346 applied balance profile method (based on the more extensive stake network). We utilized a  
347 single glacier hypsometry, derived from the 2015 DEMs, for each glacier over the entire five-  
348 year interval. Importantly, in order to facilitate a more direct comparison to the GPR-derived  
349  $B_w$  estimates, we used glaciological  $B_w$  estimates that have not been geodetically calibrated.

350

## 351 **4. Results**

### 352 **4.1. General accumulation conditions**

353 Since 1966, Wolverine Glacier's median  $B_w$  (determined from the stake network) exceeds  
354 Gulkana's by more than a factor of two (2.3 vs. 1.1 m w.e.), and exhibits greater  
355 variability, with an interquartile range more than twice as large (0.95 m w.e. vs. 0.4 m  
356 w.e.). Over the five-year study period, both glaciers experienced accumulation conditions  
357 that spanned their historical ranges, with one year in the upper quartile (including the 5<sup>th</sup>  
358 greatest  $B_w$  at Wolverine in 2016), one year within 25% of the median, and multiple years  
359 in the lower quartile (2017 at Gulkana and 2014 at Wolverine had particularly low  $B_w$   
360 values) (Fig. 2). In all years,  $B_w$  at Wolverine was greater, although in 2013 and 2014, the  
361 difference was only 0.1 m w.e.

362

363 Average accumulation season (taken as October 1 – May 31) wind speeds over the study  
364 period were stronger ( $\sim 7$  m s<sup>-1</sup> vs.  $\sim 3$  m s<sup>-1</sup>) and from a more consistent direction at  
365 Wolverine than Gulkana (northeast at Wolverine, southwest to northeast at Gulkana)  
366 (Fig. S6). On average, Wolverine experienced  $\sim 50$  days with wind gusts  $> 15$  m s<sup>-1</sup> each  
367 winter, while for Gulkana, this only occurred on  $\sim 7$  days. Over the five-year study period,  
368 interannual variability in wind direction was very low at Wolverine (2016 saw slightly  
369 greater variability, with an increase in easterly winds). In contrast, at Gulkana, winds  
370 were primarily from the northeast to east in 2013–2015, from the southwest to south in  
371 2016–2017, and experienced much greater variability during any single winter.

372

### 373 **4.2. *In situ* and GPR point observations**

374 Glacier-averaged snow densities across all years were 440 kg m<sup>-3</sup> (range 414–456 kg m<sup>-3</sup>)  
375 at Wolverine and 362 kg m<sup>-3</sup> (range 328–380 kg m<sup>-3</sup>) at Gulkana (Table S1). Average  
376 radar velocities were 0.218 m ns<sup>-1</sup> (range 0.207–0.229 m ns<sup>-1</sup>) at Wolverine and 0.223 m

377  $\text{ns}^{-1}$  (0.211–0.231  $\text{m ns}^{-1}$ ) at Gulkana. Over this five-year interval, the GPR point  
378 observations revealed a general pattern of increasing SWE with elevation, along with  
379 fine-scale variability due to wind redistribution (e.g., upper elevations of Wolverine) and  
380 localized avalanche input (e.g., lower west branch of Gulkana) (Fig. S1, S2). The  
381 accumulation season (hereafter, winter) SWE elevation gradient was steeper ( $\sim 440$  vs.  
382  $\sim 115$   $\text{mm } 100 \text{ m}^{-1}$ ) and more variable in its magnitude at Wolverine than Gulkana.  
383 Gradients ranged between 348 – 624  $\text{mm } 100 \text{ m}^{-1}$  at Wolverine, and 74 – 154  $\text{mm } 100 \text{ m}^{-1}$   
384 at Gulkana (Fig. 4). Over all five years at both glaciers, elevation explained between 50  
385 % and 83 % of the observed variability in SWE (Fig. 4).

386

### 387 **4.3. Model performance**

388 To evaluate model performance in unsampled locations of the glacier, both extrapolation  
389 approaches were run 100 times for each glacier and each year, each time with a unique,  
390 randomly selected training (75 % of aggregated observations) and test (remaining 25 %  
391 of aggregated observations) dataset. The median and standard deviation of the  
392 coefficients of determination ( $R^2$ ) from these 100 models runs are shown in Fig. 5. Model  
393 performance ranged from 0.25 to 0.75, but on average, across both glaciers and all years,  
394 was 0.56 for the MVR approach and 0.46 for the regression tree. Model performance was  
395 higher and more consistent at Wolverine, whereas 2015 and 2017 at Gulkana had test  
396 dataset  $R^2$  of  $\sim 0.4$  and 0.3, likely reflecting the lower winter SWE elevation gradients and  
397 coefficients of determination with elevation during these years (Fig. 4). The wide range  
398 in  $R^2$  across the 100 model runs reflects the variability in training and test datasets that  
399 were randomly selected. When the test dataset terrain parameter space was captured by  
400 the training dataset, a high coefficient of determination resulted, but when the test dataset  
401 terrain parameter space was exclusive, e.g., contained only a small elevation range, the  
402 model performance was typically low. This further highlights the importance of elevation  
403 as a predictor for these glaciers.

404

405 At Gulkana, the model residuals (Fig. S1) exhibited spatiotemporal consistency, with  
406 positive residuals (i.e., observed SWE exceeded modeled SWE by  $\sim 0.2$   $\text{m w.e.}$ ) at mid-  
407 elevations of the west branch, and at the very terminus of the glacier. The largest negative

408 residuals typically occurred at the highest elevations. In both cases, these locations  
409 deviated from the overall SWE elevation gradient. At Wolverine, observations at the  
410 highest elevations typically exceeded the modeled SWE, particularly in the northeast  
411 quadrant of the glacier where wind drifting is particularly prevalent (Fig. S2). Elsewhere  
412 at Wolverine, the residuals often alternated between positive and negative values over  
413 length scales of 10s to 100s of meters (Fig. S2), which we interpret as zones of scour/drift  
414 that were better captured by the regression tree models.

415

416 The beta coefficients of terrain parameters from the MVR were fairly consistent from  
417 year-to-year at both glaciers (Fig. 6). At Wolverine, elevation was the largest beta  
418 coefficient, followed by *Sb* and curvature. At Gulkana, elevation was also the largest beta  
419 coefficient, followed by curvature. Gulkana experiences much greater variability in wind  
420 direction during the winter months (Fig. S6), possibly explaining why *Sb* was either not  
421 included or had a very low beta coefficient in the median regression model. As our  
422 surveys were completed prior to the onset of ablation, terrain parameters related to solar  
423 radiation gain (notably the terms that include aspect: northness and eastness) had small  
424 and variable beta coefficients.

425

#### 426 **4.4. Spatial Variability**

427 A common approach for quantifying snow accumulation variability across a range of  
428 means is the coefficient of variation (CoV), calculated as the ratio of the standard  
429 deviation to the mean (Liston et al., 2004; Winstral and Marks, 2014). The mean and  
430 standard deviation of CoVs at Wolverine were  $0.42 \pm 0.03$  and at Gulkana,  $0.29 \pm 0.05$ ,  
431 indicating relatively lower spatial variability in SWE at Gulkana (Fig. 7). CoVs were  
432 fairly consistent across all five years, although 2017 saw the largest CoVs at both  
433 glaciers. Interestingly, 2017 had the lowest absolute spatial variability (i.e., lowest  
434 standard deviation), but also the lowest glacier-wide averages during the study period,  
435 resulting in greater CoVs.

436

437 Qualitatively, both Wolverine and Gulkana glaciers exhibited consistent spatiotemporal  
438 patterns in accumulation across the glacier surface, with elevation exerting a first-order

439 control (Fig. 8, S7, S8). Overlaid on the strong elevational gradient are consistent  
440 locations of wind scour and deposition, reflecting the interaction of wind redistribution  
441 and complex – albeit relatively stable year to year – surface topography (consisting of  
442 both land and ice topography). For instance, numerous large drifts (~2 m amplitude, ~200  
443 m wavelength) occupy the northeast corner of Wolverine Glacier, where prevailing  
444 northeasterly winds consistently redistributed snow into sheltered locations in each year  
445 of the study period (Fig. 8). The different statistical extrapolation approaches produced  
446 nearly identical  $B_w$  estimates (4 % difference on average at Wolverine and 1 % difference  
447 on average at Gulkana) (Fig. 9). The MVR  $B_w$  estimate was larger in 4 out of 5 years at  
448 Wolverine (Fig. 9), while neither approach exhibited a consistent bias at Gulkana.

449

450 Although the glacier-wide averages between these approaches showed close agreement,  
451 we explored the differences in spatial patterns by calculating a mean SWE difference  
452 map for each glacier by differencing the five-year mean SWE produced by the  
453 regression tree model from the same produced by the MVR model (Fig. 10). As such,  
454 locations where the MVR exceeded the regression tree are positive (yellow). At Gulkana,  
455 where the two approaches showed slightly better glacier-wide  $B_w$  agreement, the  
456 magnitude in individual pixel differences were substantially less than at Wolverine (e.g.,  
457 color bar scales range  $\pm 0.2$  m at Gulkana vs.  $\pm 0.5$  m at Wolverine). At Wolverine  
458 Glacier, there were three distinct elevation bands where the MVR approach predicted  
459 greater SWE, namely the main icefall in the ablation zone, a region of complex  
460 topography centered around a normalized elevation of 0.65, and lastly, at higher  
461 elevations, where both approaches predicted a series of drift and scour zones, although in  
462 sum, the MVR model predicted greater SWE.

463

464 We used two different approaches to quantify the ‘time-stability’ of spatial patterns  
465 across these glaciers. By the first metric, normalized range, we found that both glaciers  
466 exhibited very similar patterns (Fig. 11), with either ~65 or 85 % (regression tree and  
467 MVR, respectively) of the glacier area experiencing less than 25 % absolute normalized  
468 variability (Fig. 12). The  $R^2$  approach provides an alternative way of assessing the time  
469 stability of SWE, essentially determining whether SWE at each location scales with the

470 glacier-wide value. By this metric, 80 % of the glacier area at Wolverine and 96 % of the  
471 glacier area at Gulkana had a coefficient of determination greater than 0.8 (Fig. 12),  
472 suggesting that most locations on the glacier have a consistent relationship with the mean  
473 glacier-wide mass balance. By both metrics, the MVR output suggests greater ‘time-  
474 stability’ (e.g., lower normalized range or higher  $R^2$ ) compared to the regression tree.

475

#### 476 **4.5. Winter mass balance**

477 In order to examine systematic variations between the approaches we outlined in Section  
478 3 for calculating the glacier-wide winter balance,  $B_w$ , we first calculated a yearly mean  
479 from the six approaches (including four based on the GPR observations: MVR,  
480 regression tree, elevation gradient derived from centerline only observations, elevation  
481 gradient derived from all point observations, and two based on the *in situ* stake network:  
482 site-index and profile). In general, Gulkana exhibited greater agreement (4 % average  
483 difference) among the approaches, with most approaches agreeing within 5 % of the six-  
484 approach mean (Fig. 13; Table S2). Wolverine showed slightly less agreement (7 %  
485 average difference), as the two terrain parameters statistical extrapolations (MVR and  
486 regression tree) produced  $B_w$  estimates  $\sim$ 9 % above the mean, while the two stake derived  
487 estimates were  $\sim$ 7 % less than the mean. On average across all five years at Wolverine,  
488 the MVR approach was the most positive, while the glaciological site-index approach  
489 was always the most negative (Fig. 13). At both glaciers, the estimates using elevation as  
490 the only predictor yielded  $B_w$  estimates on average within 3 % of the six-method mean,  
491 with the centerline only based estimate being slightly negatively biased, and the complete  
492 observations being slightly positively biased.

493

494 To examine the systematic difference between the glaciological site-index method and  
495 GPR-based MVR approach, we compared stake-derived  $b_w$  values from the three long-  
496 term stakes to all GPR-based MVR  $b_w$  values within that index zone (Fig. 14). Both the  
497 stakes and the GPR-derived  $b_w$  values have been normalized by the glacier-wide value to  
498 make these results comparable across years and glaciers. It is apparent that Wolverine  
499 experienced much greater spatial variability in accumulation, with larger interquartile  
500 ranges and a large number of positive outliers in all index zones. Importantly, the stake



501 weight in the site-index solution is dependent on the hypsometry of the glacier, and for  
502 both glaciers, the upper stake accounts for ~65 % of the weighted average. In years that  
503 the misfit between GPR  $B_w$  and site-index  $B_w$  was largest (2015 and 2016 at Gulkana,  
504 2013 and 2017 at Wolverine), the stake-derived  $b_w$  at the upper stake was in the lower  
505 quartile of all GPR-derived  $b_w$  values, explaining the significant difference in  $B_w$   
506 estimates in these years. Potential reasons for this discrepancy are discussed in Section  
507 5.3.

508

509 *In situ* stake and pit observations traditionally serve as the primary tool for deriving  
510 glaciological mass balances. However, in order for these observations to provide a  
511 systematic and meaningful long-term record, they need to record interannual variability  
512 in mass balance rather than interannual spatial variability in mass balance. To assess the  
513 performance of the long-term stake sites, we examined the interannual variability metrics  
514 for the stake locations. By both metrics (normalized absolute range and  $R^2$ ), the middle  
515 and upper elevation stakes at both glaciers appear to be in locations that achieve this  
516 temporal stability, having exhibited ~10 % range and  $R^2 > 0.95$  over the five-year interval.  
517 The lower elevation stake was less temporally stable and exhibited opposing behavior at  
518 each glacier. At Gulkana, this stake had a high  $R^2$  (0.93) and moderate normalized  
519 variability (26 %), which in part, reflects the lower total accumulation at this site and the  
520 ability for a single uncharacteristic storm to alter this total amount significantly. In  
521 contrast, Wolverine's lowest site exhibited both low  $R^2$  ( $< 0.01$ ) and normalized range (2  
522 %), a somewhat unlikely combination. The statistical extrapolation approaches frequently  
523 predicted zero or near-zero cumulative winter accumulation at this site (i.e., mid-winter  
524 rain and/or ablation is common at this site), so although the normalized range was quite  
525 low, predicted SWE values were uncorrelated with  $B_w$  over the study interval.

526

## 527 **Discussion**

### 528 **5.1. Interannual variability in spatial patterns**

529 Each glacier exhibited consistent normalized SWE spatial patterns across the five-year  
530 study, reflecting the strong control of elevation and regular patterns in wind redistribution  
531 in this complex topography (Fig. 11, S7, S8). This is particularly notable given the highly

532 variable magnitudes of accumulation over the five-year study and the contrasting climate  
533 regions of these two glaciers (wet, warm maritime and cold, dry continental), with unique  
534 storm paths, timing of annual accumulation, wind direction and wind direction  
535 variability, and snow density. At both glaciers, the lowest interannual variability was  
536 found away from locations with complex topography and elevated surface roughness,  
537 such as crevassed zones, glacier margins, and areas near peaks and ridges.

538

539 In the most directly comparable study using repeat GPR surveys at Switzerland's  
540 Findelgletscher, 86 % of the glacier area experienced less than 25 % range in relative  
541 normalized accumulation over a three-year interval (Sold et al., 2016). As noted in  
542 Section 3.4., we reported an absolute normalized range, whereas Sold et al. (2016)  
543 reported a relative normalized range. Following their calculation, we found that 81 and  
544 82 % of Wolverine and Gulkana's area experienced a relative normalized range less than  
545 25 %. Collectively, our results add to the growing body of evidence (e.g., Deems et al.,  
546 2008; Sturm and Wagner, 2010; Schirmer et al., 2011; Winstral and Marks, 2014)  
547 suggesting 'time-stability' in the spatial distribution of snow in locations that span a  
548 range of climate zones, topographic complexity, and relief. While the initial effort  
549 required to constrain the spatial distribution over a given area can be significant, the  
550 benefits of understanding the spatial distribution are substantial and long-lasting, and  
551 have a wide range of applications.

552

### 553 **5.1.1 Elevation**

554 Elevation explained between 50 and 83 % of the observed SWE variability at Gulkana  
555 and Wolverine, making it the most significant terrain parameter at both glaciers every  
556 year (Fig. 4, 6). Steep winter SWE gradients characterized both glaciers throughout the  
557 study period (115 – 440 mm 100 m<sup>-1</sup>). Such gradients are comparable to previous results  
558 for glaciers in the region (Pelto, 2008; Pelto et al., 2013; McGrath et al., 2015), but  
559 exceed reported orographic precipitation gradients in other mountainous regions by a  
560 factor of 2–3 (e.g., Anderson et al., 2014; Grünewald and Lehning, 2011). These steep  
561 gradients are likely the result of physical processes beyond just orographic precipitation,  
562 including storm systems that deliver snow at upper elevations and rain at lower elevations

563 (common at both Wolverine and Gulkana) and mid-winter ablation at lower elevations (at  
564 Wolverine). These processes have also been shown to steepen observed SWE gradients  
565 relative to orographic precipitation gradients in a mid-latitude seasonal snow watershed  
566 (Anderson et al., 2014). Unfortunately, given that we solely sampled snow distribution at  
567 the end of the accumulation season, the relative magnitude of each of these secondary  
568 processes is not constrained.

569

570 Wolverine and Gulkana glaciers exhibited opposing SWE gradients at their highest  
571 elevations, with Wolverine showing a sharp non-linear increase in SWE, while Gulkana  
572 showed a gradual decrease. This non-linear increase was also noted at two maritime  
573 glaciers (Scott and Valdez) in 2013 (McGrath et al., 2015), and perhaps reflects an  
574 abundance of split precipitation phase storms in these warm coastal regions. The cause of  
575 the observed reverse gradient at Gulkana may be the result of wind scouring at the  
576 highest and most exposed sections of the glacier, or in part, a result of where we were  
577 able to safely sample the glacier. For instance, in 2013, when we were able to access the  
578 highest basin on the glacier, the SWE elevation gradient remained positive (Fig. 4).  
579 Reductions in accumulated SWE at the highest elevations have also been observed at  
580 Lemon Creek Glacier in southeast Alaska and Findel Glacier in Switzerland (Machguth  
581 et al., 2006), presumably related to wind scouring at these exposed elevations.

582

### 583 **5.1.2. Wind redistribution**

584 Both statistical extrapolation approaches found terrain parameters  $Sb$  and curvature,  
585 proxies for wind redistribution, to have the largest beta coefficients after elevation (Fig.  
586 6, S9). The spatial pattern of SWE estimated by each model clearly reflects the dominant  
587 influence of wind redistribution and elevation (Fig. 8), as areas of drift and scour are  
588 apparent, especially at higher elevations. However, these terms do not fully capture the  
589 redistribution process, as the model residuals (Fig. S1, S2) show sequential positive and  
590 negative residuals associated with drift/scour zones. There are a number of reasons why  
591 this might occur, including variable wind directions transporting snow (this is likely a  
592 more significant issue at Gulkana, which experiences greater wind direction variability  
593 (Fig. S6)), complex wind fields that are not well represented by a singular wind direction

594 (Dadic et al., 2010), changing surface topography (the glacier surface is dynamic over a  
595 range of temporal scales, changing through both surface mass balance processes and ice  
596 dynamics), and widely varying wind velocities. This is particularly relevant at Wolverine,  
597 where wind speeds regularly gust over  $30 \text{ m s}^{-1}$  during winter storms, speeds that result in  
598 variable length scales of redistribution that would not be captured by a fixed length scale  
599 of redistribution. All of these factors influence the redistribution of snow and limit the  
600 predictive ability of relatively simple proxies. Significant effort has gone into developing  
601 physically-based snow-distribution models (e.g., Alpine3D and SnowModel), however,  
602 high-resolution meteorological forcing data requirements generally limit the application  
603 of these models in glacierized basins. Where such observations do exist, previous studies  
604 have illuminated how the final distribution of snow is strongly correlated to the complex  
605 wind field, including vertical (surface normal) winds (Dadic et al., 2010).

606

### 607 **5.1.3. Differences with non-glaciated terrain**

608 Although our GPR surveys did not regularly include non-glaciated regions of these  
609 basins, a few key differences are worth noting. First, the length scales of variability on  
610 and off the glacier were distinctly different, with shorter scales and greater absolute  
611 variability (snow-free to  $>5 \text{ m}$  in less than  $10 \text{ m}$  distance) off-glacier (Fig. S10). This  
612 point has been clearly shown using airborne LiDAR in a glaciated catchment in the  
613 Austrian Alps (Helfricht et al., 2014). The reduced variability on the glacier is largely due  
614 to surface mass balance and ice flow processes that act to smooth the surface, leading to a  
615 more spatially consistent surface topography, and therefore a more spatially consistent  
616 SWE pattern. For this reason, establishing a SWE elevation gradient on a glacier is likely  
617 much less prone to terrain-induced outliers compared to off-glacier sites, although the  
618 relationship of this gradient to off-glacier gradients is generally unknown.

619

### 620 **5.2. Spatial differences between statistical models**

621 The two statistical extrapolation approaches yielded comparable large-scale spatial  
622 distributions and glacier-wide averages, although there were some notable spatial  
623 differences (Fig. 10). The systematic positive bias of the MVR approach over the  
624 regression tree at Wolverine was due to three sectors of the glacier with both complex

625 terrain (i.e., icefalls) and large data gaps (typically locations that are not safe to access on  
626 ground surveys). The difference in predicted SWE in these locations is likely due to how  
627 the two statistical extrapolation approaches handle unsampled terrain parameter space.  
628 The MVR extrapolates based on global linear trends, while the regression tree assigns  
629 SWE from terrain that most closely resembles the under-sampled location. Anecdotally,  
630 it appears that the MVR may overestimate SWE in some of these locations, which is most  
631 evident in Wolverine’s lower icefall, where bare ice is frequently exposed at the end of  
632 the accumulation season (Fig. S11) in locations where the MVR predicted substantial  
633 SWE. Likewise, the regression tree models could be underestimating SWE in these  
634 regions, but in the absence of direct observations the errors are inherently unknown. The  
635 regression tree model captures more short length scale variability while the MVR model  
636 clarifies the larger trends. Consequently, smaller drifts and scours are captured well by  
637 the regression tree model in areas where the terrain parameter space is well surveyed, but  
638 the results become progressively less plausible as the terrain becomes more different  
639 from the sampled terrain parameter space. In contrast, the MVR model appears to give  
640 more plausible results at larger spatial scales. This suggests that there is some theoretical  
641 threshold where the regression tree is more appropriate if the terrain parameter space is  
642 sampled sufficiently, but that for many glacier surveys the MVR model would be more  
643 appropriate.

644

### 645 **5.3. Winter mass balance comparisons**

646 On average, all methods for estimating  $B_w$  were within  $\pm 11$  % of the six-method mean,  
647 (Fig. 13). The agreement (as measured by the average percent difference from the mean)  
648 between estimates was slightly better at Gulkana than Wolverine, likely reflecting the  
649 overall lower spatial variability at Gulkana and the greater percentage of the glacier area  
650 where  $b_w$  correlates well with the glacier-wide average (Fig. 11 e, f). At both glaciers,  $B_w$   
651 solutions based solely on elevation showed excellent agreement to the six-method mean,  
652 suggesting that this simple approach is a viable means for measuring  $B_w$  on these glaciers.  
653 The biggest differences occurred between the GPR-forced MVR model and the  
654 glaciological site-index method, which we’ve shown is attributed to the upper stake (with  
655 the greatest weight) underestimating the median SWE for that index zone (Fig. 14). The

656 upper stake location was established in 1966 at an elevation below the median elevation  
657 of that index zone, which given the strong elevation control on SWE, is a likely reason  
658 for the observed difference. At Gulkana, the relationship between the upper index site  
659 and the GPR-forced MVR model is more variable in large part due to observed  
660 differences in the accumulation between the main branch (containing the index site) and  
661 the west branch of the glacier (containing additional stakes added in 2009). Such basin-  
662 scale differences are likely present on many glaciers with complex geometry, and thus  
663 illustrate potential uncertainties of using a small network of stakes to monitor the mass  
664 balance of these glaciers. In the context of the MVR model, this manifests as a change in  
665 sign in the eastness coefficient (which separates the branches in parameter space; Fig.  
666 S4). Notably, in the two years where the site-index estimate was most negatively biased  
667 at Gulkana (2015 and 2016), the glaciological profile method, relying on the more  
668 extensive stake network (which includes stakes in the west branch of the glacier), yielded  
669  $B_w$  estimates within a few percent of the GPR-derived MVR estimate.

670

671 These GPR-derived  $B_w$  results have important implications for the cumulative  
672 glaciological (stake-derived) mass balance time-series (currently only based on the site-  
673 index method), which is calibrated with geodetic observations (O’Neel et al., 2014). It is  
674 important to remember that the previous comparisons (e.g., Fig. 13) were based on  
675 glaciological  $B_w$  values that have not had a geodetic calibration applied. At Wolverine,  
676 the cumulative annual glaciological mass balance solutions are positively biased  
677 compared to the geodetic mass balance solutions over decadal timescales, requiring a  
678 negative calibration ( $-0.43$  m w.e.  $a^{-1}$ ; O’Neel et al., 2014) to be applied to the  
679 glaciological solutions. The source of this disagreement is some combination of the  
680 stake-derived winter and summer balances being too positive relative to the geodetic  
681 solution. On average, the GPR-derived  $B_w$  results were  $\sim 0.4$  m w.e. more positive than the  
682 site-index  $B_w$  results at Wolverine, which would further increase the glaciological-  
683 geodetic solution difference and suggest that the stake-derived glaciological solutions are  
684 underestimating ablation ( $B_s$ ) by  $\sim 0.8$  m w.e.  $a^{-1}$ . Preliminary observations at Wolverine  
685 using ablation wires show that some sectors of the glacier experience very high ablation  
686 rates that are not captured by the stake network (e.g., crevassed zones through enhanced

687 shortwave solar radiation gain (e.g., Pfeffer and Bretherton, 1987; Cathles et al., 2011;  
688 Colgan et al., 2016), and/or increased turbulent heat fluxes due to enhanced surface  
689 roughness), and/or ice margins (through enhanced longwave radiation from nearby snow-  
690 free land cover)). However, these results are not universal, as the assimilation of  
691 distributed GPR observations at Findelgletcher significantly improved the comparison  
692 between geodetic and modeled mass balance estimates (Sold et al., 2016), suggesting  
693 multiple drivers of glaciologic-geodetic mismatch for long-term mass balance programs.

694

### 695 **5.3.1. Implications for stake placement**

696 Understanding the spatiotemporal distribution of SWE is useful for informing stake  
697 placements and also for quantifying the uncertainty that interannual spatial variations in  
698 SWE introduce to historic estimates of glacier-wide mass balance, particularly when  
699 long-term mass balance programs rely on limited numbers of point observations (e.g.,  
700 USGS and National Park Service glacier monitoring programs; O’Neel et al., 2014;  
701 Burrows, 2014). Our winter balance results illustrate that stakes placed at the same  
702 elevation are not directly comparable, and hence are not necessarily interchangeable in  
703 the context of a multi-year mass balance record. Most locations on the glacier exhibit bias  
704 from the average mass balance at that elevation and our results suggest interannual  
705 consistency in this bias over sub-decadal time scales. As a result, constructing a balance  
706 profile using a small number of inconsistently located stakes is likely to introduce large  
707 relative errors from one year to the next.

708

709 Considering this finding, the placement of stakes to measure snow accumulation is  
710 dependent on whether a single glacier-wide winter mass balance value ( $B_w$ ) or a spatially  
711 distributed SWE field is desired as a final product. For the former, a small number of  
712 stakes can be distributed over the glacier hypsometry in areas where interannual  
713 variability is low. Alternatively, if a distributed field is desired, a large number of stakes  
714 can be widely distributed across the glacier, including areas where the interannual  
715 variability is higher. In both cases it is important to have consistent locations from year to  
716 year, although as the number of stakes increases significantly, this becomes less critical.

717

718 We assess the uncertainty that interannual variability in the spatial distribution of SWE  
719 introduces to the historic index-method (March and Trabant, 1996) mass balance  
720 solutions by first calculating the uncertainty,  $\sigma$ , contributed by each stake as:

$$721 \quad \sigma_{stake} = \sigma_{model\ residuals} + (1 - r^2) \cdot u, \quad (3)$$

722 where  $\sigma_{model\ residuals}$  is the standard deviation of MVR model residuals over all five  
723 years within  $\pm 30$  meters of the index site,  $u$  is the mean  $b_w$  within  $\pm 30$  meters of the  
724 index site, and  $R^2$  is the coefficient of determination between  $b_w$  and  $B_w$  over the five-year  
725 period (Fig. 11). The first term on the right hand side of Eq. 3 accounts for both the  
726 spatial and temporal variability in the observed  $b_w$  as compared to the model, and the  
727 second term accounts for the variability of the model as compared to  $B_w$ . The glacier-  
728 wide uncertainty from interannual variability is then:

$$729 \quad \text{Glacier } \sigma = \sqrt{\sum_{all\ stakes} (\sigma_{stake} \cdot w_{stake})^2}, \quad (4)$$

730 where  $w_{stake}$  is the weight function from the site-index method (which depends on stake  
731 location and glacier hypsometry). By this assessment, interannual variability in the spatial  
732 distribution of SWE at stake locations introduced minor uncertainty, on the order of 0.11  
733 m w.e. at both glaciers (4 % and 10 % of  $B_w$  at Wolverine and Gulkana, respectively).  
734 This suggests that the original stake network design at the benchmark glaciers does  
735 remarkably well at capturing the interannual variability in glacier-wide winter balance.  
736 The greatest interannual variability at each glacier is found at the lowest stake sites, but  
737 because  $b_w$  and the stake weights are both quite low at these sites, they contribute only  
738 slightly to the overall uncertainty. Instead, the middle and upper elevation stakes  
739 contribute the greatest amount to the glacier-wide uncertainty.

740

## 741 **6. Conclusions**

742 We collected spatially extensive GPR observations at two glaciers in Alaska for five  
743 consecutive winters to quantify the spatiotemporal distribution of SWE. We found good  
744 agreement of glacier-average winter balances,  $B_w$ , among the four different approaches  
745 used to extrapolate GPR point measurements of SWE across the glacier hypsometry.  
746 Extrapolations relying only on elevation (i.e., a simple balance profile) produced  $B_w$   
747 estimates similar to the more complicated statistical models, suggesting that this is an  
748 appropriate method for quantifying glacier-wide winter balances at these glaciers. The



749 more complicated approaches, which allow SWE to vary across a range of terrain-  
750 parameters based on DEMs, show a high degree of temporal stability in the pattern of  
751 accumulation at both glaciers, as ~85 % of the area on both glaciers experienced less than  
752 25 % normalized absolute variability over the five-year interval. Elevation and the  
753 parameters related to wind redistribution had the most explanatory power, and were  
754 temporally consistent at each site. The choice between MVR and regression tree models  
755 should depend on both the range in terrain-parameter space that exists on the glacier,  
756 along with how well that space is surveyed.

757

758 In total, six different methods (four based on GPR measurements and two based on stake  
759 measurements) for estimating the glacier-wide average agreed within  $\pm 11$  %. The site-  
760 index glaciological  $B_w$  estimates were negatively biased compared to all other estimates,  
761 particularly when the upper-elevation stake significantly underestimated SWE in that  
762 index zone. In contrast, the profile glaciological approach, using a more extensive stake  
763 network, showed better agreement with the other approaches, highlighting the benefits of  
764 using a more extensive stake network.

765

766 We found the spatial patterns of snow accumulation to be temporally stable on these  
767 glaciers, which is consistent with a growing body of literature documenting similar  
768 consistency in a wide variety of environments. The long-term stake locations experienced  
769 low interannual variability in normalized SWE, meaning that stake measurements tracked  
770 the interannual variability in SWE, rather than interannual variability in spatial patterns.  
771 The uncertainty associated with interannual spatial variability is only 4–10 % of the  
772 glacier-wide  $B_w$  at each glacier. Thus, our findings support the concept that sparse stake  
773 networks can be effectively used to measure interannual variability in winter balance on  
774 glaciers.

775

776 *Data Availability.* The GPR and associated observational data used in this study can be  
777 accessed on the USGS Glaciers and Climate Project website  
778 (<https://doi.org/10.5066/F7M043G7>). The Benchmark Glacier mass balance input and  
779 output can be accessed at: <https://doi.org/10.5066/F7HD7SRF> (O’Neel et al., 2018). The

780 Gulkana DEM is available from the ArcticDEM project website  
781 (<https://www.pgc.umn.edu/data/arcticdem/>) and the Wolverine DEM is available at  
782 <ftp://bering.gps.alaska.edu/pub/chris/wolverine/>. A generalized version of the SWE  
783 extrapolation code is available at: [https://github.com/danielmcgrathCSU/Snow-](https://github.com/danielmcgrathCSU/Snow-Distribution)  
784 Distribution.

785

786 *Author Contributions.* SO, DM, LS, and HPM designed the study. DM performed the  
787 analyses and wrote the manuscript. LS contributed to the design and implementation of  
788 the analyses, and CM, SC, and EHB contributed specific components of the analyses. All  
789 authors provided feedback and edited the manuscript.

790

791 *Competing Interests.* The authors declare that they have no conflict of interest.

792

793 *Acknowledgments.* This work was funded by the U.S. Geological Survey Land Change  
794 Science Program, USGS Alaska Climate Adaptation Science Center, and DOI/USGS  
795 award G17AC00438 to DM. Any use of trade, firm, or product names is for descriptive  
796 purposes only and does not imply endorsement by the U.S. Government. We  
797 acknowledge the Polar Geospatial Center (NSF-OPP awards 1043681, 1559691, and  
798 1542736) for the Gulkana DEM. We thank Caitlyn Florentine, Jeremy Littell, Mauri  
799 Pelto, and an anonymous reviewer for their thoughtful feedback that improved the  
800 manuscript.

801

## 802 **References**

803

804 Akaike, H.: A new look at the statistical model identification, *IEEE Trans. Autom.*  
805 *Control*, AC-19(6), 1974.

806

807 Anderson, B. T., McNamara, J. P., Marshal, H. P., and Flores, A. N.: Insights into the  
808 physical processes controlling correlations between snow distribution and terrain  
809 properties, *Water Res. Res.*, 50(6), 4545–4563, doi:10.1002/2013WR013714, 2014.

810

811 Bauder, A. (ed): *The Swis Glaciers, 2013/14 and 2014/15*, Glaciological Report (Glacier)  
812 No. 135/136, doi:10.18752/glrep\_135-136, 2017.

813

814 Bair, E. H., Calfa, A.A., Rittger, K., and Dozier, J.: Using machine learning for real-time  
815 estimates of snow water equivalent in the watersheds of Afghanistan, *The Cryosphere*,  
816 12, 1579–1594, doi:10.5194/tc-12-1579-2018, 2018.

817

818 Balk, B. and Elder, K.: Combining binary regression tree and geostatistical methods to  
819 estimate snow distribution in a mountain watershed, *Water Res. Res.*, 36(1), 13–26, 2000.

820

821 Burrows, R.: Annual report on vital signs monitoring of glaciers in the Central Alaska  
822 Network 2011-2013, Natural Resource Technical Report NPS/CAKN/NRTR—2014/905,  
823 National Park Service, Fort Collins, Colorado, 2014.

824

825 Breiman, L.: Bagging predictors, *Mach. Learn.*, 24, 123–140,  
826 <https://doi.org/10.1023/A:1018054314350>, 1996.

827

828 Breiman, L.: Random forests, *Mach. Learn.*, 45, 5–32,  
829 <https://doi.org/10.1023/A:1010933404324>, 2001.

830

831 Breiman, L., Friedman, J. H., Olshen, R. A., and Stone, C. J.: *Classification and*  
832 *Regression Trees*, Chapman and Hall, New York, 368 pp., 1984.

833

834 Cathles, L. C., Abbot, S. D., Bassis, J. N., and MacAyeal, D.R.: Modeling surface-  
835 roughness/solar-ablation feedback: application to small-scale surface channels and  
836 crevasses of the Greenland ice sheet, *Ann. Glaciol.*, 52(59), 99–108, 2011.

837

838 Cogley, J. G., Hock, R., Rasmussen, L. A., Arendt, A. A., Bauder, A., Braithwaite, R. J.,  
839 Jansson, P., Kaser, G., Möller, M., Nicholson, L. and Zemp, M.: *Glossary of Glacier*  
840 *Mass Balance and Related Terms*, IHP-VII Technical Documents in Hydrology No. 86,  
841 IACS Contribution No. 2, UNESCO-IHP, Paris, 2011.

842

843 Colgan, W., Rajaram, H., Abdalati, W., McCutchan, C., Mottram, R., Moussavi, M. S.,  
844 and Grigsby, S.: Glacier crevasses: Observations, models, and mass balance implications,  
845 *Rev. Geophys.*, 54, doi:10.1002/2015RG000504, 2016.

846

847 Dadic, R., Mott, R., Lehning, M., and Burlando, P.: Wind influence on snow depth  
848 distribution and accumulation over glaciers, *J. Geophys. Res.*, 115, F01012,  
849 doi:10.1029/2009JF001261, 2010.

850

851 Deems, J. S., Fassnacht, S. R., and Elder, K. J.: Interannual consistency in fractal snow  
852 depth patterns at two Colorado mountain sites, *J. Hydromet.*, 9, 977–988,  
853 doi:10.1175/2008JHM901.1, 2008.

854

855 Elder, K., Michaelsen, J., and Dozier, J.: Small basin modeling of snow water  
856 equivalence using binary regression tree methods, *IAHS Publ.* 228, 129–139, 1995.

857

858 Erickson, T. A., Williams, M.W., and Winstral, A.: Persistence of topographic controls  
859 on the spatial distribution of snow in rugged mountain terrain, Colorado, United States,  
860 *Water Res. Res.*, 41, W04014, doi:10.129/2003WR002973, 2005.

861

862 Escher-Vetter, H., Kuhn, M., and Weber, M.: Four decades of winter mass balance of  
863 Vernagtferner and Hintereisferner, Austria: methodology and results, *Ann. Glaciol.*,  
864 50(50), 2009.

865 Fausto, R.S., and 11 others.: A Snow Density Dataset for Improving Surface Boundary  
866 Conditions in Greenland Ice Sheet Firn Modeling, *Front. Earth Sci.*, 6(51),  
867 doi:10.3389/feart.2018.00051, 2018.

868 Fitzpatrick, N., Radić, V., and Menounos, B.: Surface energy balance closure and  
869 turbulent flux parameterization on a mid-latitude mountain glacier, Purcell Mountains,  
870 Canada, *Front. Earth Sci.*, 5(67)), doi:10.3389/feart.2017.00067, 2017.

871 Grünewald, T., and Lehning, M.: Altitudinal dependency of snow amounts in two alpine  
872 catchments: Can catchment-wide snow amounts be estimated via single snow or  
873 precipitation stations?, *Ann. Glaciol.*, 52(58), 153–158, 2011.

874 Helfricht, K., Schöber, J., Schneider, K., Sailer, R., and Kuhn, M.: Interannual  
875 persistence of the seasonal snow cover in a glacierized catchment, *J. Glaciol.*, 60(223),  
876 doi:10.3189/2014JoG13J197, 2014.

877

878 Hock, R.: Glacier melt: a review of processes and their modeling, *Prog. Phys. Geog.*, 29,  
879 362–391, doi:10.1191/0309133305pp453ra, 2005.

880

881 Hock, R., Hutchings, J. K., and Lehning, M.: Grand challenges in cryospheric sciences:  
882 toward better predictability of glaciers, snow and sea ice, *Front. Earth Sci.*, 5(64),  
883 doi:10.3389/feart.2017.00064, 2017.

884

885 Hodgkins, R., Cooper, R., Wadham, J., and Tranter, M.: Interannual variability in the  
886 spatial distribution of winter accumulation at a high-Arctic glacier (Finsterwalderbreen,  
887 Svalbard), and its relationship with topography, *Ann. Glaciol.*, 42, 243–248, 2005.

888

889 Huss, M. and Hock, R.: A new model for global glacier change and sea-level rise, *Front.*  
890 *Earth Sci.*, 3, doi:10.3389/feart.2015.00054, 2015.

891 Kaser, G., Großhauser, M., and Marzeion, B.: Contribution potential of glaciers to water  
892 availability in different climate regimes, *Proc. Natl. Acad. Sci.*, 107, 20,223–20,227,  
893 doi:10.1073/pnas.1008162107, 2010.

894

895 Klos, P. Z., Link, T. E., and Abatzoglou, J. T.: Extent of the rain-snow transition zone in  
896 the western U.S. under historic and projected climate, *Geophys. Res. Lett.*, 41, 4560–  
897 4568, doi: 10.1002/2014GL060500, 2014.

898

899 Knowles, N., Dettinger, M. D., and Cayan, D. R.: Trends in snowfall versus rainfall in  
900 the Western United States, *J. Climate*, 19, 4545–4559, 2006.

901  
902 Kovacs, A., Gow, A. J., and Morey, R. M.: The in-situ dielectric constant of polar firn  
903 revisited, *Cold Reg. Sci. Tech.*, 23, 245–256, 1995.  
904  
905 Kuhn, M.: The mass balance of very small glaciers, *Z. Gletscherkd. Glazialgeol.*, 31(1–  
906 2), 171–179, 1995.  
907  
908 Lehning, M., Grünewald, T., and Schirmer, M.: Mountain snow distribution governed by  
909 altitudinal gradient and terrain roughness, *Geophys. Res. Lett.*, 38, L19504,  
910 doi:10.1029/2011GL048927, 2011.  
911  
912 Li, L. and Pomeroy, J. W.: Estimates of threshold wind speeds for snow transport using  
913 meteorological data, *J. Applied Met.*, 36, 205-213, 1997.  
914  
915 Liston, G. E., and Elder, K.: A distributed snow-evolution modeling system  
916 (SnowModel), *J. Hydromet.*, 7, 1259-1276, 2006.  
917  
918 Littel, J. S., McAfee, S. A., and Hayward, G. D.: Alaska snowpack response to climate  
919 change: statewide snowfall equivalent and snowpack water scenarios, *Water*, 10 (5), doi:  
920 10.3390/w10050668, 2018.  
921  
922 Kjøllmoen, B. (ed), Andreassen L.M., Elvehøy, H., Jackson, M., and Melvold, J:  
923 Glaciological investigations in Norway 2016, NVE Rapport 76 2017, 108 pp, 2017.  
924  
925 Marks, D., Domingo, J., Susong, D., Link, T., and Garen, D.: A spatially distributed  
926 energy balance snowmelt model for application in mountain basins, *Hydrol. Processes*,  
927 13, 1935–1959, 1999.  
928  
929 Machguth, H., Eisen, O., Paul, F., and Hoelzle, M.: Strong spatial variability of snow  
930 accumulation observed with helicopter-borne GPR on two adjacent Alpine glaciers,  
931 *Geophys. Res. Lett.*, 33, L13503, doi:10.1029/2006GL026576, 2006.

932

933 March, R. S., and Trabant, D. C.: Mass balance, meteorological, ice motion, surface  
934 altitude, and runoff data at Gulkana Glacier, Alaska, 1992 balance year, Water-Resources  
935 Investigations Report, 95-4277, 1996.

936

937 McAfee, S., Walsh, J., and Rupp, T. S.: Statistically downscaled projections of snow/rain  
938 partitioning for Alaska, *Hydrol. Process.*, 28(12), 3930–3946, doi:10.1002/hyp.9934,  
939 2013.

940

941 McGrath, D., Sass, L., O'Neel, S., Arendt, A., Wolken, G., Gusmeroli, A., Kienholz, C.,  
942 and McNeil, C.: End-of-winter snow depth variability on glaciers in Alaska, *J. Geophys.*  
943 *Res. Earth Surf.*, 120, 1530–1550, doi:10.1002/2015JF003539, 2015.

944

945 McGrath, D., Sass, L., O'Neel, S., Arendt, A. and Kienholz, C.: Hypsometric control on  
946 glacier mass balance sensitivity in Alaska and northwest Canada, *Earth's Future*, 5, 324–  
947 336, doi:10.1002/2016EF000479, 2017.

948

949 Meromy, L., Molotch, N. P., Link, T. E., Fassnacht, S. R., and Rice, R.: Subgrid  
950 variability of snow water equivalent at operational snow stations in the western USA,  
951 *Hydro. Proc.*, 27, 2383-2400, doi:10.1002/hyp.9355, 2013.

952

953 Molotch, N. P., Colee, M. T., Bales, R. C. and Dozier, J.: Estimating the spatial  
954 distribution of snow water equivalent in an alpine basin using binary regression tree  
955 models: the impact of digital elevation data and independent variable selection, *Hydrol.*  
956 *Proc.*, 19, 1459–14-79, doi:10.1002/hyp.5586, 2005.

957

958 Nolan, M., Larsen, C., and Sturm, M.: Mapping snow depth from manned aircraft on  
959 landscape scales at centimeter resolution using structure-from-motion photogrammetry,  
960 *The Cryosphere*, 9, 1445-1463, doi:10.5194/tc-9-1445-2015, 2015.

961

962 Noh, M. J. and Howat, I. M.: Automated stereo-photogrammetric DEM generation at  
963 high latitudes: Surface Extraction with TIN-based Search-space Minimization (SETSM)  
964 validation and demonstration over glaciated regions, *GIScience & Remote*  
965 *Sensing*, 52(2), 198-217, doi:10.1080/15481603.2015.1008621, 2015.

966

967 O’Neel, S., Hood, E., Arendt, A., and Sass, L.: Assessing streamflow sensitivity to  
968 variations in glacier mass balance, *Climatic Change*, 123(2), 329–341,  
969 doi:10.1007/s10584-013-1042-7, 2014.

970

971 O’Neel, S., Fagre, D. B., Baker, E. H., Sass, L. C., McNeil, C. J., Peitzsch, E. H.,  
972 McGrath, D. and Florentine, C. E.: Glacier-Wide Mass Balance and Input Data: USGS  
973 Benchmark Glaciers, 1966-2016 (ver. 2.1, May 2018), U.S. Geological Survey data  
974 release, <https://doi.org/10.5066/F7HD7SRF>, 2018.

975

976 Painter, T., Berisford, D., Boardman, J., Bormann, K., Deems, J., Gehrke, F., Hedrick,  
977 A., Joyce, M., Laidlaw, R., Marks, D., Mattmann, C., McGurk, B., Ramirez, P.,  
978 Richardson, M., Skiles, S.M., Seidel, F., and Winstral, A.: The Airborne Snow  
979 Observatory: fusion of scanning lidar, imaging spectrometer, and physically-based  
980 modeling for mapping snow water equivalent and snow albedo, *Remote Sens. Environ.*,  
981 184, 139–152, doi:10.1016/j.rse.2016.06.018, 2016.

982

983 Pelto, M.: Utility of late summer transient snowline migration rate on Taku Glacier,  
984 Alaska, *The Cryosphere*, 5, 1127–1133, doi:10.5194/tc-5-1127-2011, 2011.

985

986 Pelto, M., Kavanaugh, J., and McNeil, C.: Juneau Icefield Mass Balance Program  
987 1946–2011, *Earth Syst. Sci. Data*, 5, 319-330, [https://doi.org/10.5194/essd-5-319-](https://doi.org/10.5194/essd-5-319-2013)  
988 2013, 2013.

989

990 Pérez-Ruiz, M., Carballido, J., and Agüera, J.: Assessing GNSS correction signals for  
991 assisted guidance systems in agricultural vehicles, *Precision Agric.*, 12, 639–652,  
992 doi:10.1007/s11119-010-9211-4, 2011.



993  
994 Pfeffer, W. T., and Bretherton, C.: The effect of crevasses on the solar heating of a  
995 glacier surface, *IAHS Publ.*, 170, 191–205, 1987.  
996  
997 Pfeffer, W. T., et al.: The Randolph Glacier Inventory: A globally complete inventory of  
998 glaciers, *J. Glaciol.*, 60(221), 537–552, doi:10.3189/2014JoG13J176, 2014.  
999  
1000 Schirmer, M., Wirz, V., Clifton, A., and Lehning, M.: Persistence in intra-annual snow  
1001 depth distribution: 1. Measurements and topographic control, *Water Resour. Res.*, 47,  
1002 W09516, doi:10.1029/2010WR009426, 2011.  
1003  
1004 Sold, L., Huss, M., Hoelzle, M., Anderegg, H., Joerg, P., and Zemp, M.:  
1005 Methodological approaches to infer end-of-winter snow distribution on alpine glaciers, *J.*  
1006 *Glaciol.*, 59(218), 1047–1059, doi:10.3189/2013JoG13J015, 2013.  
1007  
1008 Sold, L., Huss, M., Machguth, H., Joerg, P. C., Vieli, G. L., Linsbauer, A., Salzmann, N.,  
1009 Zemp, M. and Hoelzle, M.: Mass balance re-analysis of Findelengletscher, Switzerland;  
1010 Benefits of extensive snow accumulation measurements, *Front. Earth Sci.*, 4(18),  
1011 doi:10.3389/feart.2016.00018, 2016.  
1012  
1013 Sturm, M. and Wagner, A. M.: Using repeated patterns in snow distribution modeling:  
1014 An Arctic example, *Water Res. Res.*, 46 (12), doi:10.1029.2010WR009434, 2010.  
1015  
1016 Van Beusekom, A. E., O’Neel, S., March, R. S., Sass, L., and Cox, L. H.: Re-analysis of  
1017 Alaskan Benchmark Glacier mass balance data using the index method, U.S. Geological  
1018 Survey Scientific Investigations Report 2010–5247, 16 p., 2010.  
1019

1020 Vincent, C., Fischer, A., Mayer, C., Bauder, A., Galos, S.P., Funk, M., Thibert, E., Six,  
1021 D., Braun, L., and Huss, M.: Common climatic signal from glaciers in the European Alps  
1022 over the last 50 years, *Geophys. Res. Lett.*, 44, 1376–1383, doi:10.1002/2016GL072094,  
1023 2017.

1024  
1025 Winstral, A., Elder, K., and Davis, R. E.: Spatial snow modeling of wind-redistributed  
1026 snow using terrain-based parameters, *J. Hydrometeo.*, 3, 524–538, 2002.

1027  
1028 Winstral, A., Marks, D. and Gurney, R.: Simulating wind-affected snow accumulations at  
1029 catchment to basin scales, *Adv. Water Res.*, 55, 64–79,  
1030 doi:10.1016/j.advwatres.2012.08.011, 2013.

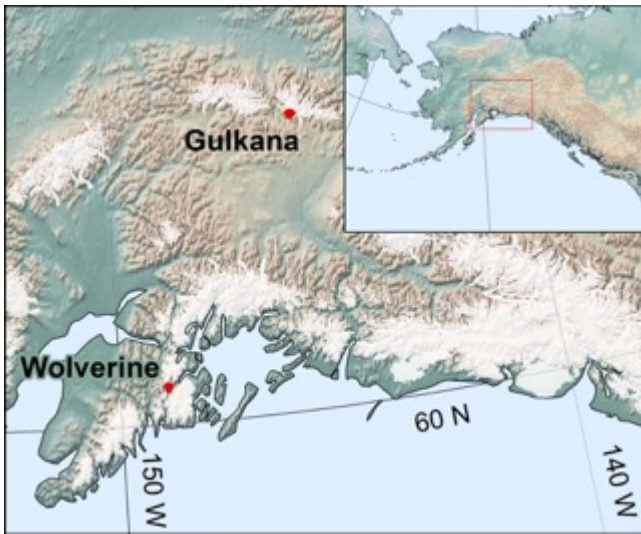
1031  
1032 Winstral, A. and Marks, D.: Long-term snow distribution observations in a mountain  
1033 catchment: Assessing variability, time stability, and the representativeness of an index  
1034 site, *Water Res. Res.*, 50, 293–305, doi:1002/2012WR013038, 2014.

1035  
1036 Woo, M.-K., and Marsh, P.: Analysis of error in the determination of snow storage for  
1037 small high Arctic basins, *J. Appl. Meteorol.*, 17, 1537–1541, 1978.

1038  
1039 Yelf, R. and Yelf, D.: Where is true time zero?, *Electro. Phenom.*, 7(1), 158–163, 2006.

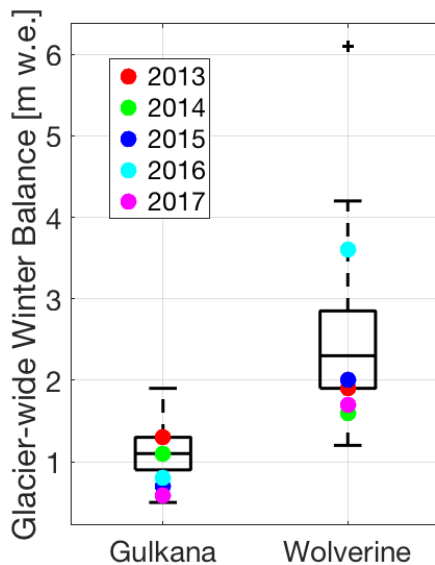
1040  
1041  
1042  
1043  
1044  
1045  
1046  
1047  
1048  
1049  
1050  
1051  
1052  
1053  
1054

1055 Figure 1. Map of southern Alaska with study glaciers marked by red outline. All glaciers  
1056 in the region are shown in white (Pfeffer et al., 2014).



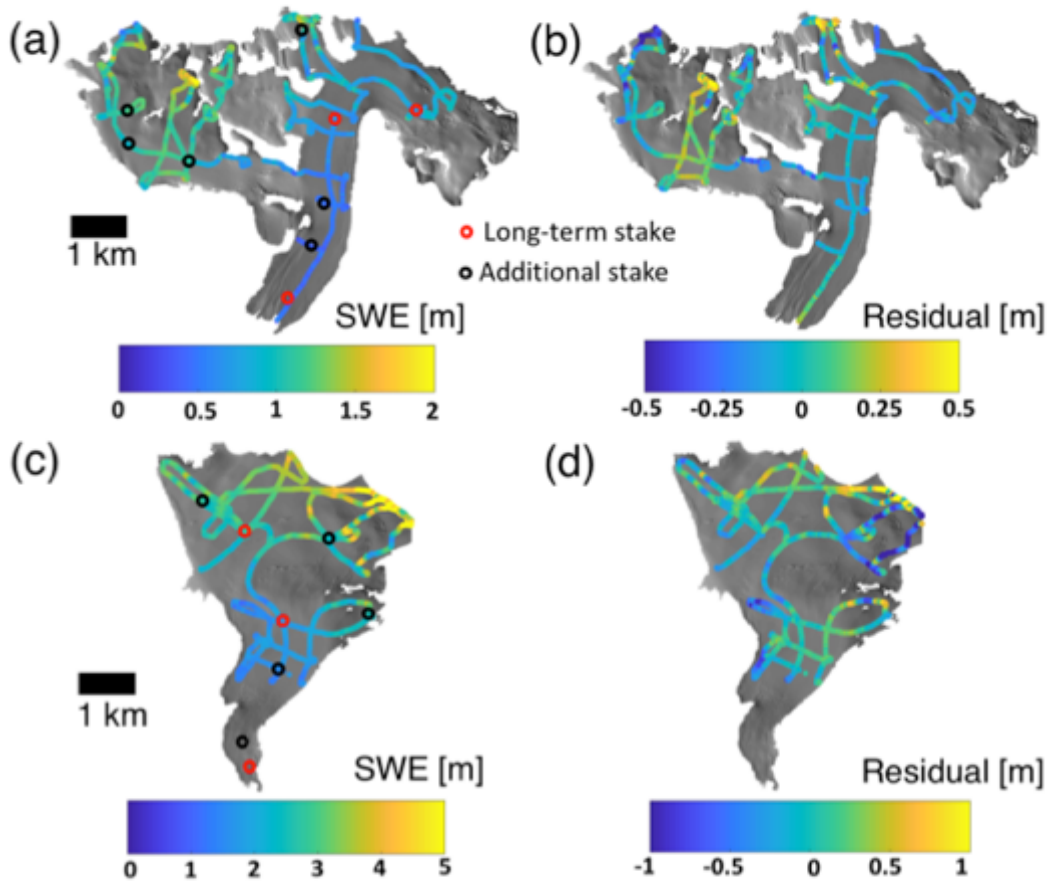
1057  
1058  
1059  
1060  
1061

1062 Figure 2. Boxplots of glacier-wide winter balance for Gulkana and Wolverine glaciers  
1063 between 1966 and 2017. Years corresponding to GPR surveys are shown with colored  
1064 markers. These values have not been adjusted by the geodetic calibration (see O’Neel et  
1065 al., 2014).



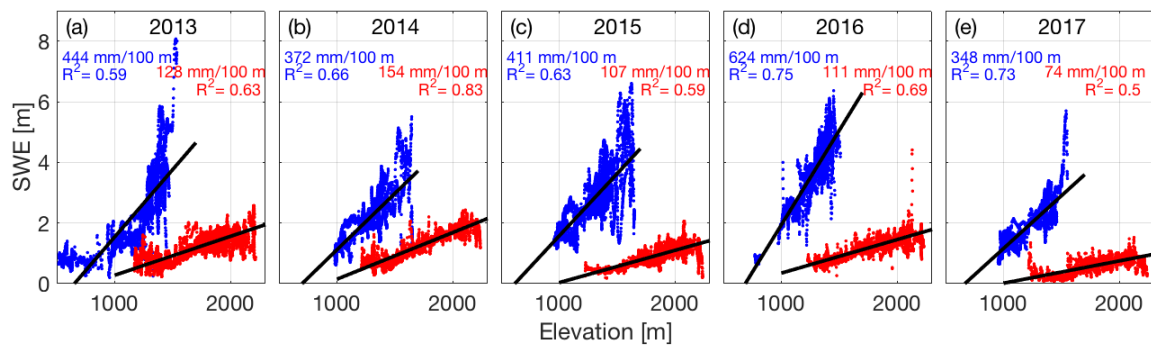
1066  
1067  
1068  
1069

1070 Figure 3. GPR surveys from 2015 at Gulkana (a) and Wolverine (c) glaciers and MVR  
 1071 model residuals (b, d).



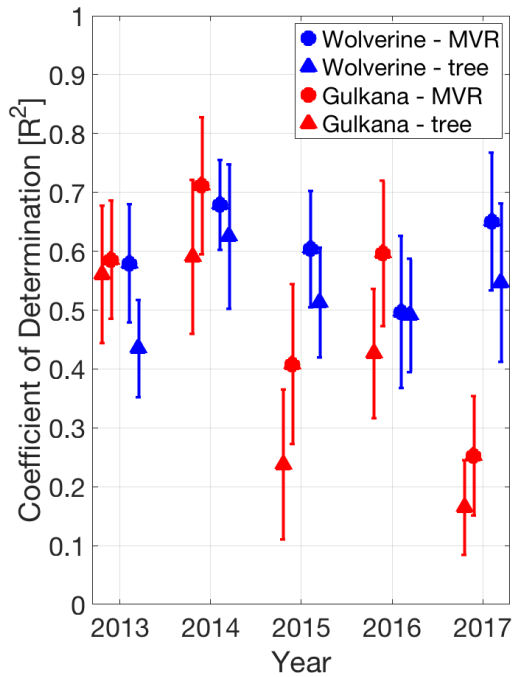
1072  
 1073  
 1074

1075 Figure 4. SWE from GPR surveys as a function of elevation, along with least squares  
 1076 regression slope and coefficient of determination for each year of the study period.  
 1077 Wolverine is plotted in blue, Gulkana in red.



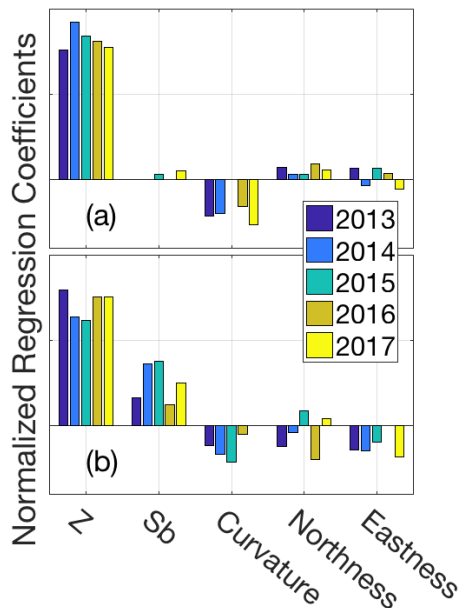
1078  
 1079

1080 Figure 5. Median and standard deviation (error bars) of coefficient of determination  
 1081 (from 100 model runs) for both extrapolation approaches (circles are MVR, triangles are  
 1082 regression tree) developed on training datasets and applied to test datasets. Symbols and  
 1083 error bars are offset from year for clarity.



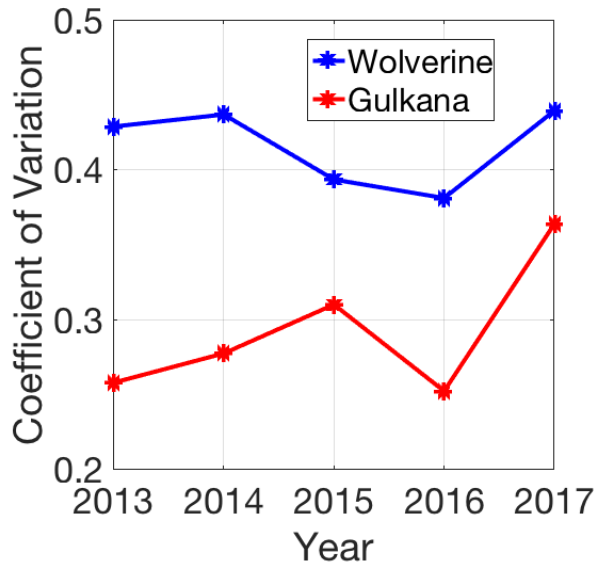
1101

1102 Figure 6. Terrain parameter beta coefficients for (a) Gulkana and (b) Wolverine for  
 1103 multivariable linear regression for each year of the study interval.



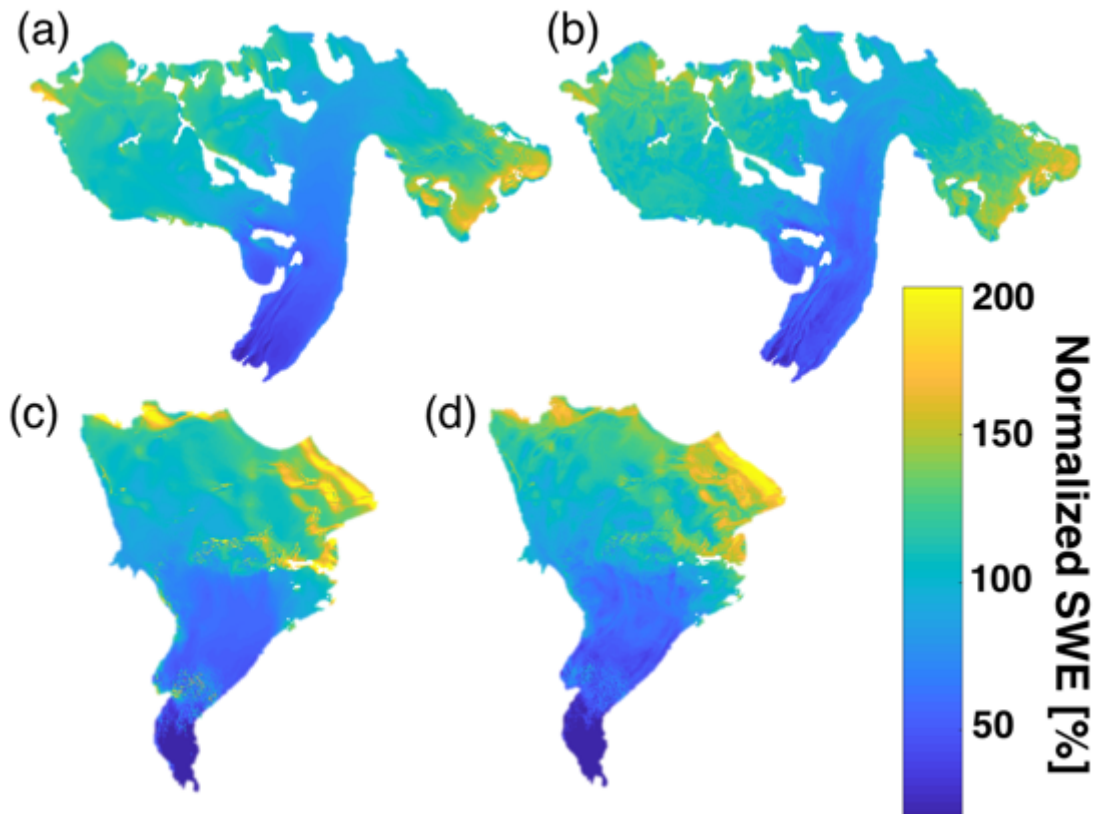
1104

1105 Figure 7. Spatial variability in snow accumulation across the glacier quantified by the  
1106 coefficient of variation (standard deviation/mean) for each glacier across the five-year  
1107 interval based on MVR model output.  
1108



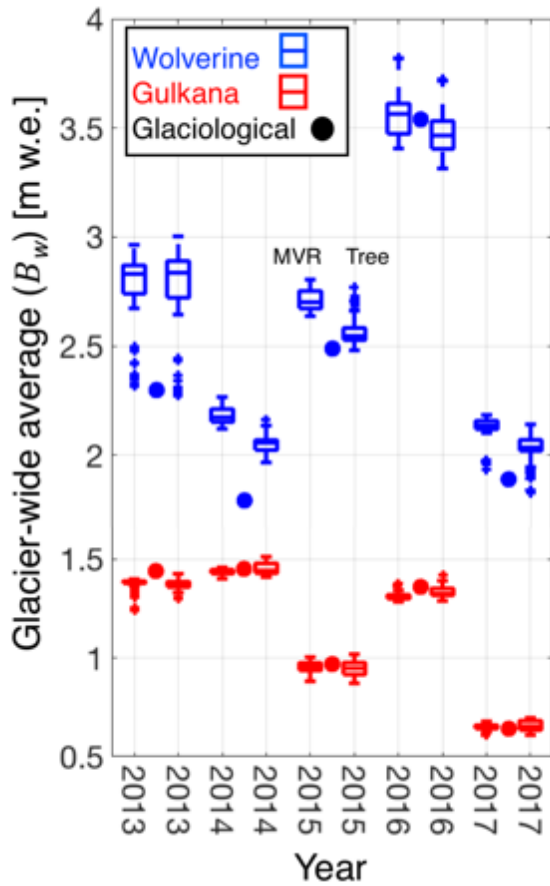
1109  
1110

1111 Figure 8. Five-year mean of normalized distributed SWE for Gulkana (a,b) and  
1112 Wolverine (c,d) for multivariable regression (a,c) and regression tree (b,d).



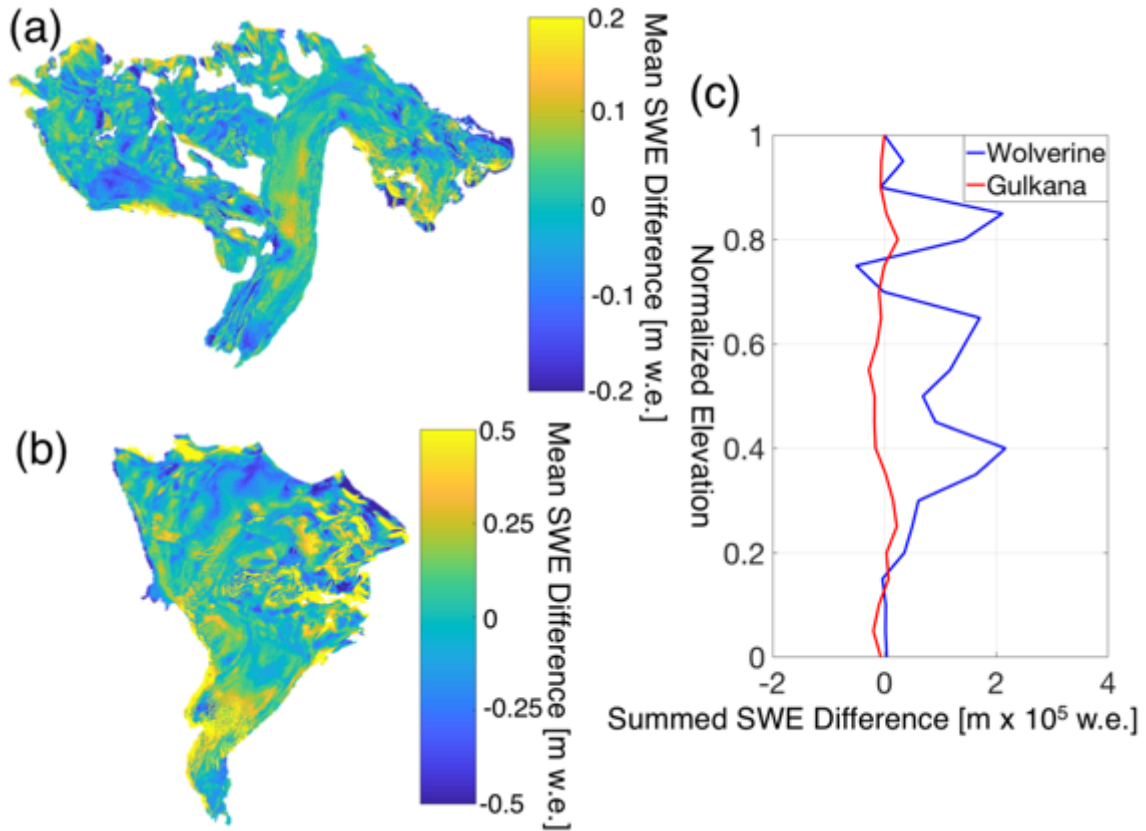
1113

1114 Figure 9. Comparing statistical models for GPR-derived glacier-wide winter balances for  
 1115 both Wolverine (blue) and Gulkana (red) glaciers. For each year and each glacier, two  
 1116 boxplots are shown. The first shows multivariable regression model (MVR) output and  
 1117 the second shows regression tree output (tree). The  $B_w$  estimate from the glaciological  
 1118 profile method is shown for each year and glacier as the filled circle.  
 1119



1120  
 1121  
 1122  
 1123  
 1124  
 1125  
 1126  
 1127  
 1128  
 1129  
 1130

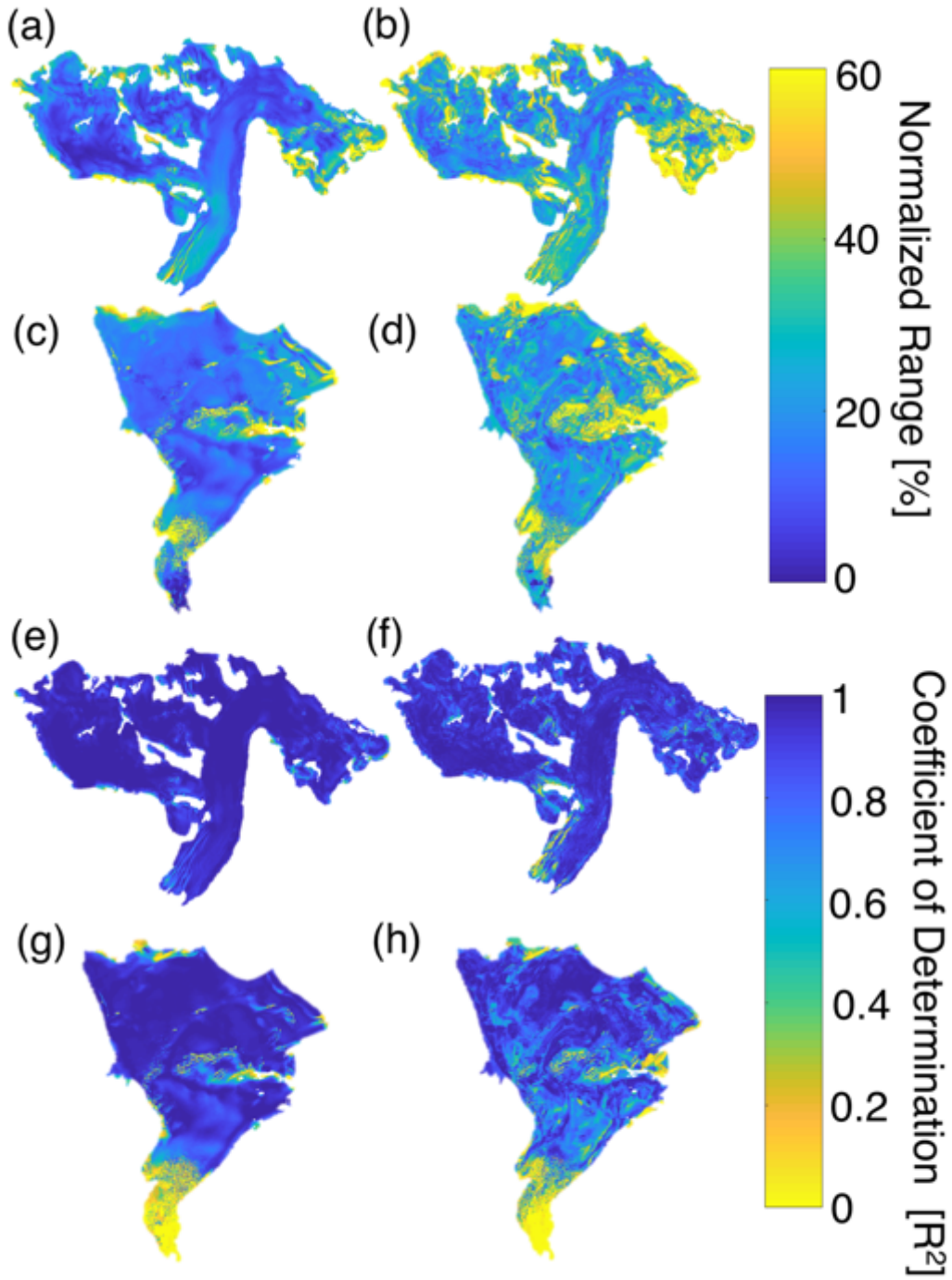
1131 Figure 10. SWE differences between statistical models for Gulkana (a) and Wolverine  
1132 (b) calculated by differencing the regression tree five-year mean SWE from the  
1133 multivariable regression (MVR) five-year mean SWE. Yellow colors indicate regions  
1134 where MVR yields more SWE than decision tree and blue colors indicate the opposite.  
1135 Note different magnitude colorbar scales. c) Summed SWE difference between methods  
1136 in bins of 0.05 normalized elevation values.



1137  
1138  
1139  
1140  
1141  
1142  
1143  
1144  
1145  
1146  
1147  
1148  
1149  
1150

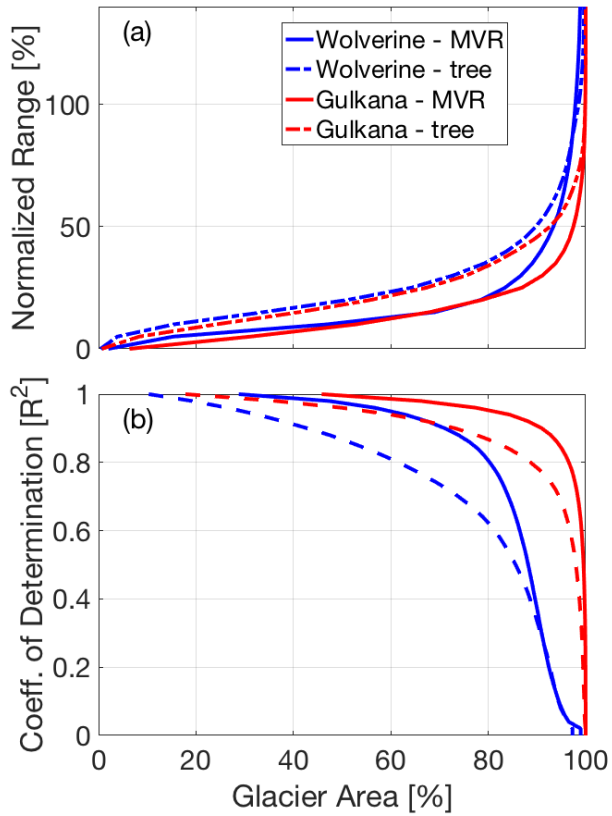


1151 Figure 11. Interannual variability of the SWE accumulation field from 2013–2017,  
1152 quantified via normalized range (a-d) and  $R^2$  (e-h) approach for median distributed fields  
1153 from the multivariable regression (left column) and regression tree (right column)  
1154 statistical models.



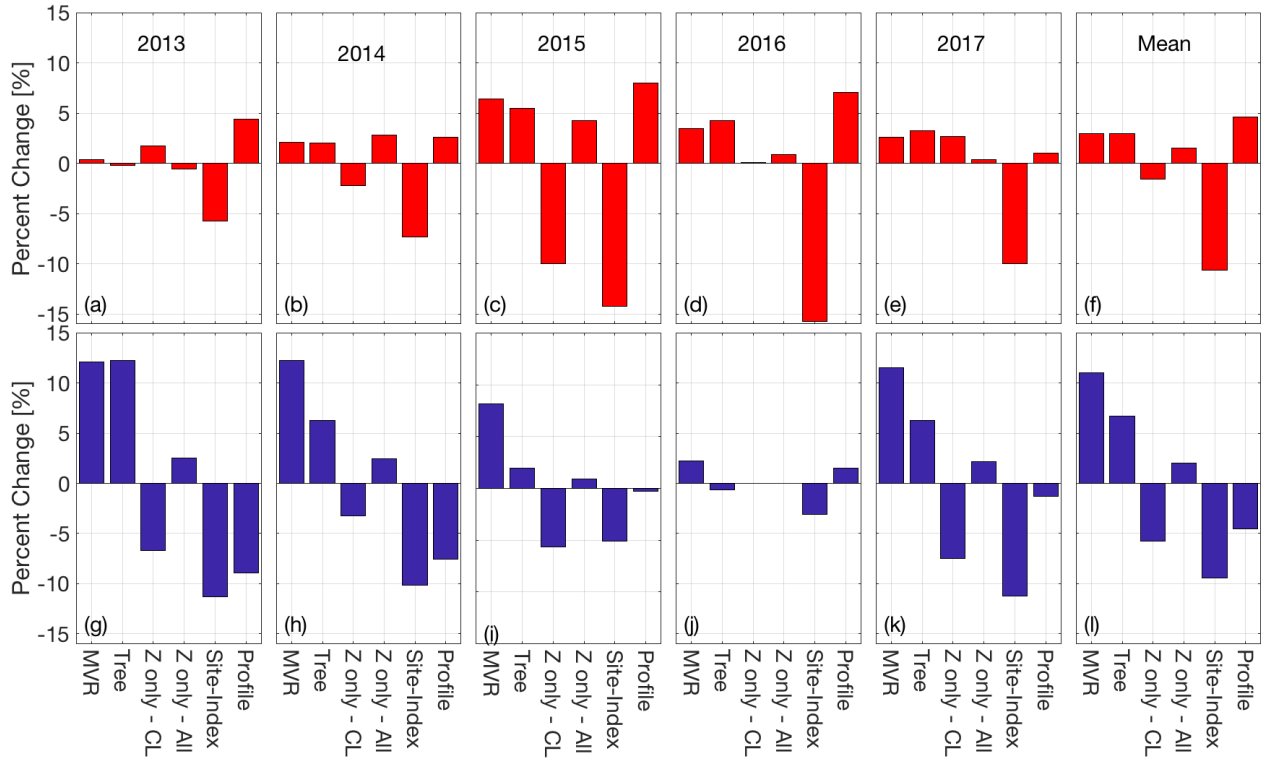
1155  
1156

1157 Figure 12. Interannual variability of the SWE accumulation pattern as a function of  
1158 cumulative glacier area, shown as (a) normalized range and (b) and  $R^2$ . Solid lines are for  
1159 multivariable regression (MVR) and dashed lines are regression tree.  
1160



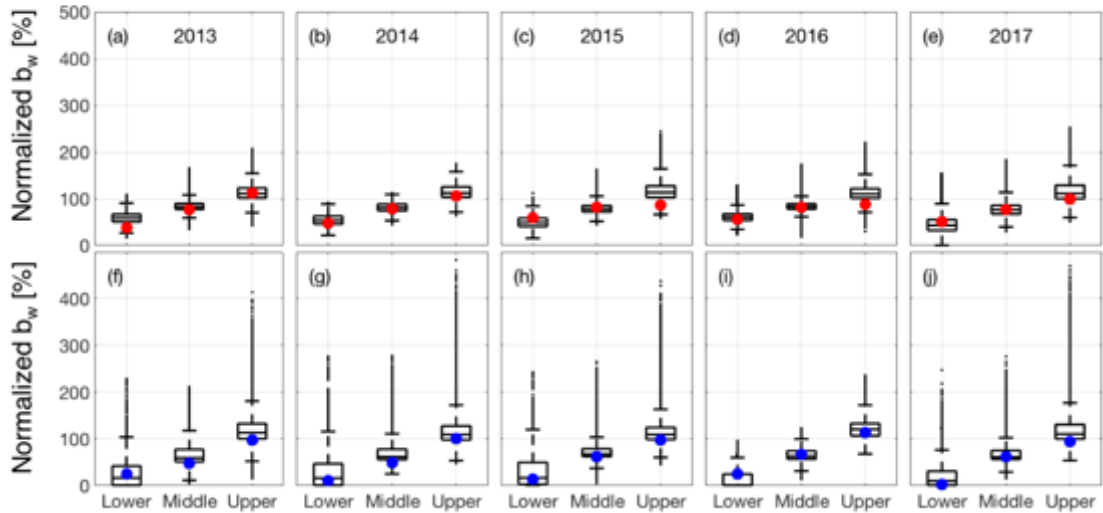
1161  
1162  
1163  
1164  
1165  
1166  
1167  
1168  
1169  
1170  
1171  
1172  
1173  
1174  
1175

1176 Figure 13. Percent deviation for each estimate from the six-method mean of  $B_w$ .  
 1177 Individual years for Gulkana Glacier are shown in panels a-e with the five-year mean  
 1178 shown in f. Individual years for Wolverine Glacier are shown in panels g-k, with the five-  
 1179 year mean shown in l.



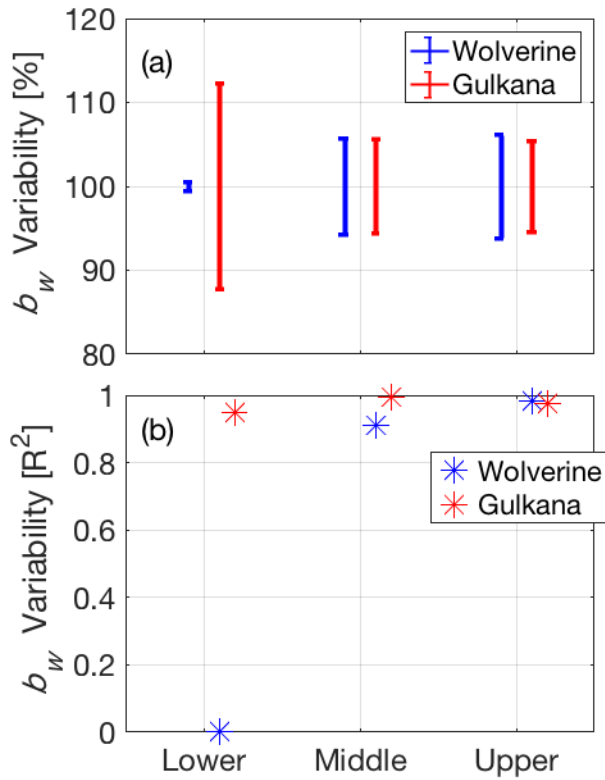
1180  
 1181  
 1182  
 1183  
 1184  
 1185  
 1186  
 1187  
 1188  
 1189  
 1190  
 1191  
 1192  
 1193  
 1194  
 1195

1196 Figure 14. Spatial variability in snow accumulation for individual years (2013-2017) by  
 1197 elevation (lower, middle, upper) compared to stake measurements. Box plot of all  
 1198 distributed SWE values (from multivariable regression) for each index zone of the glacier  
 1199 for Gulkana (a-e) and Wolverine (f-j) for 2013-2017. The filled circles are the respective  
 1200 stake observation for that index zone. SWE is expressed as a percentage of the glacier-  
 1201 wide average,  $B_w$ , for that year and glacier.



1202  
 1203  
 1204  
 1205  
 1206  
 1207  
 1208  
 1209  
 1210  
 1211  
 1212  
 1213  
 1214  
 1215  
 1216  
 1217  
 1218  
 1219  
 1220  
 1221

1222 Figure 15. Interannual variability in the spatial pattern of snow accumulation at long-term  
 1223 mass balance stake locations for Wolverine and Gulkana glaciers using a) normalized  $b_w$   
 1224 range and b) coefficient of determination (from Figure 11; MVR model).  
 1225



1226  
 1227  
 1228  
 1229  
 1230  
 1231  
 1232  
 1233  
 1234  
 1235  
 1236  
 1237